DOI: 10.1002/ ((please add manuscript number))
Article type: Full paper

Fe_2O_3-TiO_2 nano-heterostructure photoanodes for highly efficient solar water oxidation

By *Michael E.A. Warwick, Giorgio Carraro, Chiara Maccato, Alberto Gasparotto, Kimmo Kaunisto, Cinzia Sada, Stuart Turner, Yakup Gönüllü, Tero-Petri Ruoko, Laura Borgese, Elza Bontempi, Gustaaf Van Tendeloo, Helge Lemmetyinen, Sanjay Mathur and Davide Barreca**

Dr. M.E.A. Warwick, Dr. G. Carraro, Prof. C. Maccato, Dr. A. Gasparotto
Department of Chemistry, Padova University and INSTM, 35131 Padova, Italy.

Dr. K. Kaunisto, Mr. T.-P. Ruoko, Prof. H. Lemmetyinen
Department of Chemistry and Bioengineering, Tampere University of Technology, 33101 Tampere, Finland.

Prof. C. Sada
Department of Physics and Astronomy, Padova University, 35131 Padova, Italy.

Dr. S. Turner, Prof. G. Van Tendeloo
EMAT, University of Antwerp, 2020 Antwerpen, Belgium.

Dr. Y. Gönüllü, Prof. S. Mathur
Department of Chemistry, Chair of Inorganic and Materials Chemistry, Cologne University, 50939 Cologne, Germany.

Dr. L. Borgese, Prof. E. Bontempi
Chemistry for Technologies Laboratory, Brescia University, 25123 Brescia, Italy.

[*] Dr. D. Barreca
CNR-IENI and INSTM - Department of Chemistry, Padova University, 35131 Padova, Italy.
E-mail: davide.barreca@unipd.it

Keywords: Fe_2O_3; TiO_2; nano-heterostructures; water splitting; PEC.

Abstract: Harnessing solar energy for the production of clean hydrogen by photoelectrochemical (PEC) water splitting represents a very attractive, but challenging approach for sustainable energy generation. In this regard, we report on the fabrication of Fe_2O_3-TiO_2 photoanodes, showing record-breaking performances (≈10.0 mA/cm^2 at 1.8 V *vs.* RHE in 1 M NaOH) under simulated one-sun illumination. This goal, corresponding to a 10-fold photoactivity enhancement with respect to bare Fe_2O_3, is achieved by atomic layer deposition (ALD) of TiO_2 layers over *hematite* (α-Fe_2O_3) nanostructures fabricated by plasma enhanced-chemical vapor deposition (PE-CVD), and final annealing at 650°C. The adopted approach enables an intimate TiO_2-Fe_2O_3 coupling, resulting in an electronic interplay at the TiO_2/Fe_2O_3 interface. The reasons for the photocurrent enhancement determined by TiO_2 overlayers with increasing thickness are unraveled by a detailed chemico-physical investigation, as well as by the study of photogenerated charge carrier dynamics. Transient absorption analysis show retarded electron-hole recombination in an ultrafast timescale and enhanced electron extraction for TiO_2-Fe_2O_3 systems, increasing thus the number of carriers participating in water splitting. The obtainment of stable responses even in simulated seawater provides a feasible route in view of the eventual large-scale generation of renewable energy.

1. Introduction

The development of sustainable energy systems has become an ever-growing demand with the rising stress of the global population, standard of living and increased industrialization.[1-7] In this context, photo-activated methods such as photoelectrochemical (PEC) H_2O splitting, starting from solar photons and water, the most abundant natural resources, are environmentally benign alternatives for the sustainable production of hydrogen as a clean and renewable fuel, addressing thus the open energy challenge.[8-23]. A key issue for PEC water splitting is the identification of suitable photoanodes satisfying the main requirements for solar hydrogen production.[13-14,24-25] Among the most promising candidates, *hematite* (α-Fe_2O_3) has long been a preferred choice[18-19,21,26-28] thanks to its good photochemical stability, earth abundance, non-toxicity, low cost and proper band gap ($E_G \approx$ 2.1 eV) to absorb a large fraction of the solar spectrum.[3-4,16,22,29-33] In spite of these advantages, the solar-to-hydrogen efficiency based on *hematite* falls well short of the theoretical maximum (≈13%)[6-7,10-11,31,34] due to a number of factors,[2,12,17,24,35-36] including poor transport properties, improper band positions for unassisted water splitting, low electron-hole pair lifetime (< 10 ps) and small exciton diffusion length (≈2-4 nm).[11,27,32,37-39]. In order to overcome these drawbacks and enhance *hematite* conductivity and photoresponses, the most commonly used strategies include nanoarchitecture engineering[7,11,19,23,25,35,37] and introduction of various dopants into Fe_2O_3 lattice.[17-18,24,28,40-42] Other improvements have been afforded by the introduction of oxygen evolution catalysts (OECs), such as Co, Ir- and Ru-based ones.[1,10,20,24-25,35] Despite the advantageous reduction in the onset potential, most of these systems are rare and/or expensive, being unsuitable for large-scale energy production, and water oxidation efficiencies are often limited by surface recombination, a severe issue to be tackled.[20,25,43] In order to address the primary requirements for an efficient solar-to-hydrogen conversion, an alternative strategy consists of the formation of nano-heterostructures involving Fe_2O_3 coupling with both under-

or overlayers,[1,4,30,38,44-45] to suppress electron back-recombination at the *hematite*/substrate interface,[21,27-28] enhance light absorption and improve charge carrier transport properties.[5,16,20,26,46] So far, various works have been focused on the surface functionalization of Fe_2O_3 nanosystems with various oxides, such as Al_2O_3, Ga_2O_3, $Fe_xSn_{1-x}O_4$, and TiO_2.[3,10,20-21,37] The obtained results highlight the possibility of improving PEC performances by passivation of surface states, protection against corrosion, use of buried semiconductor junctions,[2,20] and a proper tailoring of charge transfer processes between the constituent phases.[21,46] Nevertheless, the practical use of modified *hematite* photoanodes in efficient, durable, and inexpensive solar hydrogen production is still hindered by various factors,[34] including the system stability[28] and the difficulties in identifying precise structure-functions relationships.[6,17] In addition, driving PEC water splitting more efficiently than the state-of-the-art *hematite* photoanodes[35,47] remains an actual key hurdle impeding further technological developments.[31]

In the present study, we report on a method for the enhancement of *hematite* photoanode charge transfer, resulting in a remarkable improvement of the recorded PEC performances in water splitting activated by solar irradiation. Basing on a previous work on surface functionalization of nanostructured Fe_2O_3 polymorphs for self-cleaning applications,[48] we have devoted our attention to the coating of PE-CVD *hematite* nanostructures by an ALD TiO_2 overlayer, followed by thermal treatment in air at 650°C. It is worth highlighting that, despite several efforts have been aimed at investigating Ti incorporation into *hematite* photoelectrodes,[7,13,18,28,32-34,36,38-39,41-43,46,49] Fe_2O_3-TiO_2 multi-layered and composite systems have been much less investigated so far.[3,6,16,26,44] For these materials, the current density for water photooxidation has been reported to drop off with an increased number of TiO_2 ALD cycles, the reasons underlying this behavior being unclear.[2] In this work, taking advantage of ALD repeatability, conformality and precise thickness control at low deposition temperatures,[45,48] we focus on the PEC behavior of Fe_2O_3-TiO_2 nano-heterostructures

characterized by a different thickness of TiO_2 overlayers. A relevant attention is devoted to the interrelations between system properties and functional performances, with particular regard to the structural and electronic interplay occurring at TiO_2/Fe_2O_3 heterointerfaces. Under optimized conditions, a 10-fold increase in the registered photocurrent compared to bare PE-CVD α-Fe_2O_3 photoanodes was observed, corresponding to the highest performances ever reported for similar systems, especially at high applied potentials. This feature, along with the high system stability even in simulated seawater, for which solar splitting has only been seldom investigated,[29] represents a key issue towards the sustainable and efficient conversion of solar light into chemical energy.

2. Results and Discussion

2.1 Preparation and Characterization of Fe_2O_3-TiO_2 photoanodes

Fe_2O_3-TiO_2 photoanodes were fabricated by a three-step protocol, involving: i) PE-CVD of Fe_2O_3 by on Fluorinde-doped Tin Oxide (FTO) substrates; ii) ALD of TiO_2 overlayers with a different cycle numbers, in order to tailor the corresponding overlayer thickness, and iii) annealing in air for 1 h at 650°C (Table 1).

The fabricated Fe_2O_3 systems [Supporting Information (SI), Figure S1], composed of pure α-Fe_2O_3 (*hematite*) free from other iron oxide polymorphs, were characterized by an inherently porous nano-organization. The subsequent ALD of TiO_2 overlayers on these systems resulted in the occurrence of morphological variations, as can be appreciated by the pertaining field emission-scanning electron microscopy (FE-SEM) micrographs (see Figure 1). In particular, specimens **400_L** and **400_H**, obtained with a lower and a higher number of ALD cycles in TiO_2 deposition, presented more rounded surface features than bare Fe_2O_3 (compare SI, Figures S1a-b), suggesting the homogeneous formation of continuos TiO_2 overlayers conformally covering the underlying Fe_2O_3 nanostructures. Whereas in the case of **400_L** functionalization with TiO_2 did not lead to significant alterations of the pristine Fe_2O_3 aggregate features,

indicating the formation of a conformal thin film, for specimen **400_H** more marked modifications of the surface morphology took place (Figures 1a-b). The occurrence of multi-layered structures was clearly evidenced by of cross-sectional FE-SEM images (Figures 1c-d), highlighting that uniform titanium dioxide layers were deposited over the pristine iron oxide nanostructures. As can be noticed, upon going from specimen **400_L** to the homologous **400_H**, *i.e.*, upon increasing the number of ALD cycles, the TiO_2 overlayer thickness underwent a parallel enhancement. These observations, along with the intimate and uniform Fe_2O_3-TiO_2 contact, highlight the intrinsic ALD conformal coverage capability,[19-20,48] enabling a fine control of the resulting Fe_2O_3-TiO_2 heterojunction features. Cross sectional FE-SEM images enabled to estimate the total nanodeposit (titania overlayer) thickness values, yielding 400 ± 15 (36 ± 10) and 480 ± 30 (80 ± 10) nm for **400_L** and **400_H**, respectively. In order to attain a further insight into the material topography, the material surfaces were probed by atomic force microscopy (AFM; Figures 1g-h). The recorded micrographs showed the formation of multi-grain structures with the various aggregates well interconnected between themselves, in line with FE-SEM observations. The obtainment of very similar Root-Mean-Square (RMS) roughness values (≈20 nm) irrespective of the synthesis conditions suggested that the eventual differences in the system PEC behaviour were almost independent from their surface areas, as discussed in detail below.

The local in-depth composition was analysed by energy dispersive X-ray spectroscopy (EDXS) line-scans (Figures 1e-f). The obtained data showed that TiO_2 was mainly concentrated in the outermost material region, a phenomenon more evident for the **400_H** sample, confirming that a higher number of ALD cycles resulted in a thicker TiO_2 overlayer, as already appreciated by FE-SEM images. Conversely, the FeKα line intensity underwent a progressive increase in the inner system region at expenses of the TiKα one, confirming thus the predominance of Fe_2O_3 in the deposit regions closer to the FTO substrate.

Since the mutual vertical distribution of Fe_2O_3 and TiO_2 is a key issue for an optimal heterostructure engineering, the in-depth chemical composition along the thickness was further investigated by secondary ion mass spectrometry (SIMS) analyses (Figures 2a-b). The obtained data enabled to estimate a mean C concentration (averaged over the whole thickness) as low as 150 ppm, hihlighting thus the purity of the obtained materials. Irrespective of the processing conditions, the O ionic yield remained almost constant throughout the investigated depth. As observed, the outermost sample region was Ti-rich, a phenomenon particularly evident for specimen **400_H**, characterized by a higher thickness of the TiO_2 overlayer. Upon increasing the sputtering time, a concomitant increase in the Fe ionic yield and a progressive decrease in the Ti one took place, with no net drop-off of the titianium signal. This evidence suggested that the TiO_2 layer was covering the Fe_2O_3 nanostructures even in the inner regions, a phenomenon due to the sinergy between the Fe_2O_3 porosity and the good conformality achievable by the use of ALD. Finally, both titanium and iron signals underwent a drop-off at the interface with the FTO substrate. The Sn tailing extending into the nanodeposits at the interfacial region suggested the occurrence of tin diffusion from the FTO substrate induced by thermal annealing, at least to some extent. This phenomenon, already observed in previous works, might result beneficial for PEC performances, due to an improved system electrical conductivity.[34,50-51]

Overall, the data discussed so far point out to the obtainment of bi-layered Fe_2O_3-TiO_2 heterostructures, with titanium oxide being mainly confined in the outermost system regions. To perform a detailed characterization of the Fe and Ti chemical environments, X-ray photoelectron spectroscopy (XPS) analyses were carried out. Wide-scan XPS spectra (SI, Figure S2a) were characterized by titanium and oxygen photopeaks. In the case of sample **400_L**, the surface presence of iron could also be detected (see Figure 2d), indicating only a partial coverage of the underlying Fe_2O_3 matrix upon TiO_2 deposition. Irrespective of the used ALD conditions, the $Ti2p_{3/2}$ Binding Energy (BE) of 458.5 eV, as well as the separation between the spin-orbit components [Δ(BE) = 5.7 eV] (Figure 2c), were in line with the

presence of Ti(IV) in TiO_2.[32,52] The Fe2p peak shape and position [Figure 2d; BE($Fe2p_{3/2}$) = 711.1 eV], along with the pertaining spin-orbit splitting [Δ(BE) = 13.7 eV], were consistent with the formation of iron(III) oxide free from other Fe oxidation states.[7,11,30,32,42,52] The O1s profile (Figure S3b) could be fitted by two contributing bands located at BE = 530.0 eV (I) and 531.8 eV (II), attributed to lattice O and surface chemisorbed –OH groups/adsorbed oxygen.[4,7,32,42]

The structure of the deposited TiO_2-Fe_2O_3 photoanodes was investigated by X-ray diffraction (XRD). The recorded patterns (SI, Figure S3) were dominated by a series of signals correponding to *hematite* reflections for both specimens **400_L** and **400_H**.[53] Interestingly, the latter showed also the appearance of additional peaks at 2ϑ = 25.3 and 48.1°, related to (101) and (200) crystallographic planes of *anatase* TiO_2.[54] In accordance with XPS results, no reflections related to Fe-Ti-O ternary phases were present, and the absence of appreciable angular shifts also enabled to rule out the occurrence of Ti doping into Fe_2O_3, at least in an appreciable amount.

In order to investigate the nanoscale structure of Fe_2O_3-TiO_2 materials, (high resolution)-transmission electron microscopy (HR)-TEM, high angle annular dark field-scanning transmission electron microscopy (HAADF-STEM) and EDXS analyses were carried out. Figures 3a-b display HAADF-STEM (*Z*-contrast) overview images of both samples in cross-section, together with EDXS elemental maps for Ti, Fe, Sn and Si, evidencing the glass/FTO/α-Fe_2O_3/TiO_2 multi-layer stacks. The Fe_2O_3/TiO_2 interface is imaged in more detail in Figures 3c-f, enabling to extract TiO_2 overlayer thickness values in excellent agreement with those provided by FE-SEM analyses (see above and Figure 1). Irrespective of the used ALD conditions, the Fe_2O_3 nanodeposit presented well-developed upward growing Fe_2O_3 needles, whose assembly resulted in an open, porous structure. This peculiar texture enabled the ALD TiO_2 coating to be deposited even in the inner system regions. In line with the above discussed data (compare Figures 1-2), EDXS maps showed that TiO_2 covered the entire surface of Fe_2O_3

needles, providing an extended interface between both materials and confirming the formation of Fe_2O_3-TiO_2 nano-heterostructures. The overlayers, composed by TiO_2 with the *anatase* crystal phase, are further imaged by the HR micrographs reported in Figures 3g-h. As a matter of fact, the thinner overlayer in specimen **400_L** displayed a low crystallinity, explaining the absence of *anatase* signals in the corresponding XRD pattern and the appearance of only weak reflections in electron diffraction (ED) experiments (see SI, Figures S3-S4). Interestingly, small voids with a mean size of few nanometers were observed in the *titania* top layer of both Fe_2O_3-TiO_2 samples. These voids are imaged as a dark contrast in the mass-thickness sensitive HAADF-STEM view in ~~Figure 3h.~~ Figure 3h.

The target Fe_2O_3/TiO_2 hetero-nanostructures were also analyzed by optical absorption spectroscopy (SI, Figure S5). The absorption spectra were characterized by a sub-band-gap scattering tail in the 600–750 nm region, and a sharp absorbance increase occuring from 550–600 nm towards lower wavelengths, consistently with the band-gap of *hematite*.[24,38,51] As a whole, the optical properties of the present Fe_2O_3-TiO_2 heterostructures are appealing for PEC water splitting triggered by solar irradiation, since these photoanodes can efficiently absorb a significant fraction of the Vis spectrum. From Tauc plots, it was possible to extrapolate a mean band gap (E_G) value of 2.1 eV, revealing that the TiO_2 ovelayers did not significantly affect the optical features in the Vis range, as already reported.[16-17,36,43]

2.2 PEC investigation of Fe_2O_3-TiO_2 photoanodes

The functional properties of Fe_2O_3-TiO_2 heterostructures in PEC water splitting were evaluated in NaOH aqueous solution (Figure 4a) and compared with those of a bare Fe_2O_3 photoelectrode free from TiO_2 overlayers. In the absence of illumination, the samples showed very small photocurrents ($j \approx 10^{-3}$ mA/cm^2) in the potential range 0.2–1.8 V *vs.* the Reversible Hydrogen Electrode (RHE), until the current onset potential (E_{onset}) for water oxidation reaction was reached at ≈1.75 V.[5] Upon simulated solar illumination, a net j increase at

potentials lower than $E°$ (1.23 V vs. RHE) took place, since a part of the energy required for the oxidation process is captured from the incident light.[5] Considering E_{onset} as the value at which a current density of 0.02 mA/cm^2 is first reached,[6] for the pure Fe_2O_3 photoanode E_{onset} was estimated to be 1.1 V_{RHE}. Subsequently, a progressive j increase with V occurred, reaching a value of 0.24 mA/cm^2 at 1.23 V_{RHE}. As can be observed, the functionalization of *hematite* with TiO_2 overlayers resulted in a decrease of the onset potential and in a significant increase of the recorded photocurrent values. Interestingly, a dependence of PEC performances on TiO_2 thickness could be clearly appreciated, since sample **400_H** displayed a systematic enhancement of photocurrent values with respect to the **400_L** one. In particular, **400_H** showed an E_{onset} value as low as 0.8 V_{RHE} and j = 2.0 mA/cm^2 at 1.23 V_{RHE}, a value nearly ten times higher than that pertaining to pure Fe_2O_3 (**Fe_2O_3**). It is generally accepted that the required overpotential is related to the poor oxygen evolution reaction (OER) kinetics and to the unfavorable conduction band energy position for bare Fe_2O_3.[5-6,20,45] As a consequence, the shift of E_{onset} to more cathodic potentials highlights the beneficial effect exerted by TiO_2 functionalization on the system photoresponse. Along with the onset potential, one of the most important parameters to evaluate photoanode performances is represented by the photocurrent value plateau. In this regard, an important feature of the present systems is the absence of saturation at potentials higher than 1.23 V_{RHE}, indicating a more efficient charge separation upon illumination thanks to the presence of TiO_2 overlayers on Fe_2O_3.[5] To this regard, at 1.8 V_{RHE} a j value close to 10 mA/cm^2 was recorded for the **400_H** specimen. As a matter of fact, such a photocurrent threshold is the highest ever reported in the literature so far for Fe_2O_3-TiO_2 photoelectrodes.[4,6,14-15,20,29] These unprecedented photocurrent values, obtained without the use of any expensive/toxic co-catalyst, represent indeed a new frontier for solar water splitting promoted by Fe_2O_3-TiO_2 materials.

In order to further elucidate the influence of the TiO_2 overlayer, solar-to-hydrogen (STH) efficiency values were calculated from j-V data. It is worth noticing that only a few works

reporting the calculation of STH values are available in the literature.[31] As can be appreciated from Figure 4b, the STH efficiency curves followed the same trend of the *j*-V ones, and the maximum of the efficiency increased in the order: **Fe_2O_3** (0.007 %) < **400_L** (0.060 %) < **400_H** (0.098 %). Notably, the highest photoefficiency values were obtained for TiO_2-containing specimens at lower V_{RHE} values than for bare Fe_2O_3, highlighting again the active catalytic role played by *titania* functionalization on the ultimate PEC performances.

It is well know that the main drawbacks related to the use of Fe_2O_3 photoanodes include the high density of surface states, low hole mobility, short charge carrier lifetime and slow OER kinetics.[2,29] On the other hand, even TiO_2 photoanodes suffer from various disadvantages, and, in particular, from a poor solar light harvesting.[3,44] So far, some studies have demonstrated that functionalization of Fe_2O_3 with TiO_2 often results in worse PEC performances with respect to bare iron(III) oxide.[2,20,29] In a different way, the very high photocurrents shown by the present Fe_2O_3/TiO_2 photoanodes, along with the decreased onset voltages and the absence of significant saturation at high applied potentials, highlight the potential offered by Fe_2O_3/TiO_2 heterojunctions in affording favorable photoactivity improvements.[3,16,26,46] Due to the mutual positions of Fe_2O_3 and TiO_2 conduction band edges, electrons photogenerated in TiO_2 can be easily transferred to Fe_2O_3, injected into the FTO substrate and subsequently migrate through the external electric circuit to reduce water at the cathode,[44] suppressing thus detrimental recombination effects (see also below and Scheme 1). Another favorable contribution to the actual performances is related to the fact that TiO_2 overlayers can efficiently prevent *hematite* photocorrosion in a wide pH range.[5] Last but not least, the porosity of the TiO_2 overlayers, evidenced by the above presented TEM data, results in a higher contact area with the electrolyte and in a larger number of active surface states for water oxidation, that have a remarkable beneficial effect on the ultimate PEC behavior.

Basing on these very favorable premises, the most efficient photoelectrode (**400_H**) was tested in PEC water splitting using simulated seawater solutions. As a matter of fact, the use

of seawater represents a key technological target for a real-world sustainable hydrogen energy generation, since 97.5% of the overall H_2O available on earth is salt water.[55-57] Figure 4c displays *j*-V curves obtained using simulated seawater upon solar light illumination. Despite the performances are not as high as in the case of NaOH solutions, appreciable photocurrents values ($j \approx 0.4$ mA/cm^2 at 1.23 V_{RHE}) were obtained. This result, along with the previous PEC data, shows that the present Fe_2O_3-TiO_2 materials represent a key step forward for the fabrication of photoanodes to be used in real devices.

2.3 TAS analysis on Fe_2O_3-TiO_2 photoanodes

In order to further elucidate the role of Fe_2O_3/TiO_2 heterojunctions in promoting the PEC water splitting and investigate charge carrier dynamics in the target photoelectrodes, transient absorption spectroscopy (TAS) analyses were carried out. TAS measurements allow the monitoring of photogenerated electron and hole dynamics from a picosecond to a second timescale,[58-60] being a powerful tool to study the interplay between nanostructure and PEC response in Fe_2O_3 and TiO_2-based photoanodes.[24,42,58,61-62] In this work, the evolution of charge carriers was examined by using band-gap excitation of both Fe_2O_3 and TiO_2 at λ = 355 nm, simulating the solar illumination conditions, in which light is absorbed by both components.

Figure 5a presents normalized transient absorption decays for the bare *hematite* and **400_L** specimens on a 0-100 ps timescale monitored at λ = 580 nm (see also SI, Figure S6), assigned to the absorption of photogenerated charges. The selected probe wavelength corresponds to electrons trapped in *hematite* intra-band states and long-lived holes in both *hematite* and titania.[58-59,63] The retarded electron-hole recombination on the 1-10 ps time range for Fe_2O_3-TiO_2 was attributed to the passivation of Fe_2O_3 surface defect by TiO_2 deposition, resulting, in turn, in an enhancement of charge carrier separation, decreasing detrimental recombination events.[6]

The inset in Figure 5a compares the longest-lived spectrally resolved transient state, having lifetime (τ) over the experimental delay time of 6 ns, of both specimens, obtained by exponential fitting of raw data (see also SI, Figure S7). The transient spectrum of **400_L** had two main differences with respect to the bare *hematite*: *i)* a higher signal amplitude throughout the monitored range, and *ii)* an enhanced transient absorption around 500 nm. The strong absorption in the 550-700 nm wavelength range could be associated to an increased number of photogenerated charges surviving recombination on a timescale of < 10 ps, as already discussed. The enhanced absorption at λ = 500 nm was related to holes in the TiO_2 overlayer and turned out to be the most pronounced on longer timescales, suggesting an efficient hole transfer to TiO_2 in the Fe_2O_3-TiO_2 heterostructures.

To investigate the electron mobility of TiO_2-functionalized specimens, microsecond-to-millisecond TAS decays were measured at λ = 580 nm. Exponential fits of transient absorption traces for both specimens are displayed in the inset of Figure 5b (see also SI, Figure S8). The initial photobleaching, *i.e.* the negative absorption change, following the excitation laser pulse could be assigned to the intra-band trapped electrons in *hematite*.[58] The bi-exponential fits resulted in lifetimes of 0.5 and 550 ms for sample **400_L**, and 1.7 and 900 ms for bare Fe_2O_3, respectively. The short-lived components correspond to the bleaching recovery, attributed to the extraction of trapped electrons, and are therefore indicative of electron mobility in the metal oxide structure. The increased bleaching recovery rate ($1/\tau$) of **400_L** with respect to bare Fe_2O_3 indicated an enhanced electron mobility of the Fe_2O_3-TiO_2 heterostructure. The long-lived components with the positive absorption were assigned to holes participating in water oxidation, and are resolved more accurately in a millisecond-to-second timescale, in which water splitting has been reported to occur.[58,64]

The TAS decays of both specimens in a seconds time range at a probe wavelength of λ = 650 nm, corresponding the hole absorption in both Fe_2O_3 and TiO_2,[59,63] were fitted with an

exponential model, shown in Figure 5b (see also Figure S9 for raw data). Functionalization of Fe_2O_3 with the TiO_2 overlayer decreased the lifetime of long-lived photoholes, as indicated by the mean lifetimes of 1.8 and 3.0 s obtained for the **400_L** and bare Fe_2O_3 photoanodes, respectively. This phenomenon is in good agreement with the higher PEC response of the TiO_2-covered specimen, as it demonstrates the enhanced catalytic activity of the photoanode surface. It is worthwhile observing that previously published hole lifetimes for water oxidation over TiO_2 photoelectrodes are close to 0.3 s.[62,64] Hence, despite the presence of the TiO_2 overlayer. the catalytic properties of specimen **400_L** are directly influenced by the presence of the underlying *hematite*. This phenomenon is related to the fact that both Fe_2O_3 and TiO_2 are exposed on the system surface, as observed by XPS analyses (compare Figure 2), and are thus in contact with the electrolyte.

In addition, TAS analyses in a millisecond-to-second timescale were performed on sample **400_H** (SI, Figure S9), yielding a photohole lifetime of 0.5 s, close to the literature value of 0.3 s for water oxidation over bare TiO_2 (see above). This finding demonstrates the "bulk" nature of the 50 nm TiO_2 overlayer on the studied *hematite* systems and rationalizes the further enhanced PEC water splitting of the specimen with the thicker TiO_2 layer. That is, the uniform TiO_2 coverage over **400_H** yields the elevated catalytic efficiency of the photoanode with respect to **400_L**, having both Fe_2O_3 and TiO_2 components in contact with the electrolyte, due to the inherently high catalytic activity of TiO_2.

To rationalize the obtained data, it is necessary to consider that the lower valence band energy of TiO_2 with respect to Fe_2O_3 potentially prohibits hole transfer from Fe_2O_3 to TiO_2,[65] and this phenomenon should lead to a decreased PEC response. However, as demonstrated by Figure 4 and the related discussion, the photoactivity of TiO_2-functionalized specimens (**400_L** and **400_H**) significantly outperforms that of the bare *hematite* (**Fe_2O_3**). Such a remarkable PEC enhancement demonstrates an efficient charge carrier separation upon coupling the two components in the resulting Fe_2O_3-TiO_2 heterostructure. The role of the latter under high

anodic biases (>E_{onset}) can be illustrated by analyzing the energy band diagram presented in Scheme 1.[58-59,66] The system Fermi level energy decreases with increasing positive bias, which further promotes band bending phenomena. We propose that high photocurrents are achieved only after the valence band energy of *hematite* shifts to lower values with respect to the TiO_2 valence band edge at the electrolyte interface, facilitating thus hole transfer from Fe_2O_3 to TiO_2. That is, the high PEC response for the TiO_2-functionalized specimens are due to the synergistic concurrence of various effects: *a)* enhanced charge dynamics in the Fe_2O_3-TiO_2 heterostructure; *b)* increased catalytic activity of the photoanode surface due to functionalization with titania overlayers, and *c)* efficient charge transfer between Fe_2O_3 and TiO_2 at bias potentials > E_{onset}. Moreover, band bending enhances spatial charge separation, inducing a thermodynamic driving force for holes and electrons that overcomes the energy barriers at the TiO_2/Fe_2O_3 junction (Scheme 1).

3. Conclusions

In conclusion, we have successfully prepared Fe_2O_3-TiO_2 nano-heterostructure photoanodes on FTO by an original synthetic strategy, consisting of the initial growth of Fe_2O_3 nanosystems by PE-CVD followed by ALD growth of TiO_2 layers with variable thickness and thermal annealing in air. The inherent benefits of the adopted joint process have enabled the fabrication of high-purity systems, characterized by an intimate contact between Fe_2O_3 and TiO_2. These features synergistically contributed to the extremely high performances in photoelectrochemical water oxidation activated by solar illumination, that corresponded to ≈10.0 mA/cm^2 water oxidation current at 1.8 V *vs.* RHE under simulated 1-sun irradiation. The dramatic amplification in the PEC performance with respect to the case of bare Fe_2O_3 is attributed to the creation of Fe_2O_3-TiO_2 heterojunctions, resulting in a retarded electron-hole recombination in the ultrafast timescale and enhanced electron extraction to the external electrical circuit. A further contributing effect is related to the increased catalytic efficiency of

photoanodes with TiO_2 overlayers, as also demonstrated by the corresponding lower E_{onset} values.

In addition, TiO_2 protective action against corrosion has enabled to obtain attractive preliminary results even for PEC tests run in seawater, whose use in solar water splitting is reported for the first time from Fe_2O_3-TiO_2 systems. These results, along with the high and stable photoanode activity, provide a key milestone for a sustainable energy generation starting from abundant and renewable natural resources and pave the way to cost-effective hetero-nanostructure devices for solar energy conversion. Additionally, the proposed strategy and, in particular, the surface functionalization using ALD-deposited layers, may open doors to the use of combined synthesis approaches in the fabrication of a variety of nanostructures for photo-assisted applications displaying improved functionalities.

4. Experimental Section

4.1 Synthesis

Fe_2O_3 nanodeposits were fabricated by PE-CVD using a custom-built two-electrode PE-CVD apparatus [Radio Frequency (RF) = 13.56 MHz; electrode diameter = 9 cm; inter-electrode distance = 6 cm].[40] Depositions were performed on previously cleaned[40,67] FTO-coated glass substrates (Aldrich, 735167-1EA, ≈ 7 Ω/sq; lateral dimensions = 2.0 cm × 1.0 cm; FTO thickness ≈ 600 nm). Iron(III) oxide systems were deposited starting from $Fe(hfa)_2TMEDA$ (hfa = 1,1,1,5,5,5 - hexafluoro - 2,4 - pentanedionate; TMEDA = *N*,*N*,*N'*,*N'* - tetramethylethylenediamine), synthesized as previously reported.[68] In a typical growth experiment, 0.30 ± 0.01 g of precursor powders were placed in an external glass reservoir, heated by an oil bath at 65°C, and transported into the reaction chamber by electronic grade Ar [flow rate = 60 standard cubic centimeters per minute (sccm)]. In order to prevent undesired precursor condensation phenomena, connection gas lines were maintained at 140°C by means of external heating tapes. Two additional gas inlets were used for the independent

introduction of electronic grade Ar and O_2 (flow rates = 15 and 20 sccm, respectively) directly into the reaction chamber. After preliminary optimization experiments, each deposition was carried out for 1 h under the following conditions: growth temperature = 400°C; total reactor pressure = 1.0 mbar; RF-power of 10 W.

The as-prepared Fe_2O_3 nanodeposits were subsequently coated with TiO_2 layers having different thickness by means of ALD. ALD experiments were performed at a deposition temperature of 150°C by a Ultratech/Cambridge Nanotech Inc Savanna 100 machine operating between 13-15 mbar, in continuous flow mode at 20 sccm. Titanium oxide was deposited starting from titanium(IV) tetra-isopropoxide [$Ti(O^iPr)_4$] and milliQ water (H_2O) as Ti and O sources, respectively. $Ti(O^iPr)_4$ was purchased from STREM Chemicals, Inc. (France) and used without any further purification. MilliQ water was produced by means of a Millipore DirectQ-5 purification system starting from tap water. The precursors were injected in the reactor directly from stainless steel reservoirs maintained at 80°C [$Ti(O^iPr)_4$] and 25°C (H_2O). Electronic grade nitrogen was used as carrier to feed the precursors vapours alternatively into the reaction chamber. To avoid precursor condensation, both valves and delivery lines were maintained at 115 C. After preliminary optimization experiments, the cycle number was varied in order to obtain TiO_2 overlayers with tunable thickness (Table 1). After deposition, thermal treatments were carried out in air for 1 h at atmospheric pressure using a Carbolite HST 12/200 tubular furnace (heating rate = 20°C×min^{-1}) at 650°C. The use of higher temperatures was discared, in order to prevent detrimental thermal degradations of FTO substrates.[51]

4.2 Characterization

FE-SEM analyses were carried out using a Zeiss SUPRA 40 VP FE-SEM instrument equipped with an Oxford INCA x-sight X-ray detector for EDXS investigation, operating at primary beam acceleration voltages comprised between 5.0 and 10.0 kV.

AFM analyses were run using a NT-MDT SPM Solver P47H-PRO instrument operating in semicontact/tapping mode and in air. After plane fitting, RMS roughness values were obtained from 3×3 μm^2 images.

SIMS investigation was performed by means of a IMS 4f mass spectrometer (Cameca) using a Cs^+ primary beam (voltage = 14.5 keV; current = 25 nA, stability = 0.2%) and negative secondary ion detection, adopting an electron gun for charge compensation. Beam blanking mode and high mass resolution configuration were adopted. Signals were recorded rastering over a 150×150 μm^2 area and detecting secondary ions from a sub-region close to 10×10 μm^2 in order to avoid crater effects.

XRD measurements were conducted operating in reflection mode by means of a Dymax-RAPID microdiffractometer equipped with a cylindrical imaging plate detector, allowing data collection from 0 to 160° (2ϑ) horizontally and from -45 to +45° (2ϑ) vertically upon using CuKα radiation (λ = 1.54056 Å). Each pattern was collected with an exposure time of 40 min, using a collimator diameter of 300 μm. Conventional XRD patterns were obtained by integration of 2D images.

TEM, HAADF-STEM and EDXS mapping experiments were carried out on a FEI Tecnai Osiris microscope, operated at 200 kV and equipped with a Super-X high solid angle energy-dispersive X-ray detector, as well as a FEI Titan "cubed" microscope (acceleration voltage = 200 kV), equipped with an aberration corrector for the probe-forming lens and a Super-X high solid angle EDXS detector.

XPS analyses were run on a Perkin-Elmer Φ 5600ci apparatus with a standard AlKα radiation ($h\nu$ = 1486.6 eV), at operating pressures < 10^{-8} mbar. Charge correction was performed by assigning to the adventitious C1s signal a Binding Energy (BE) of 284.8 eV.[69] After a Shirley-type background subtraction, atomic percentages (at. %) were calculated by signal integration using standard PHI V5.4A sensitivity factors.

Optical absorption spectra were recorded in transmission mode at normal incidence by means of a Cary 50 spectrophotometer, using bare FTO glass as a reference. In all cases, the substrate contribution was subtracted. Tauc plots were performed basing on Tauc equation, assuming the occurrence of direct allowed transitions.[40]

PEC measurements were performed in un-buffered NaOH solutions (pH = 13.6) and simulated seawater solutions (0.5 m NaCl) **YAKUP is it this correct?** using a saturated calomel electrode (SCE) as reference, a Pt wire as counter-electrode and the TiO_2/α-Fe_2O_3 nanodeposits as working electrodes. A copper wire was soldered on an uncovered portion of the FTO substrate to establish electrical connection, and an epoxy resin was used to seal all exposed FTO portions, except for the electrode working areas.[49] Prior to measurements, the electrolyte was purged with nitrogen in order to prevent any possible reaction with dissolved oxygen. Linear sweep voltammetry (10 mV/s) was carried out between -1.0 and 1.0 V *vs.* SCE using a potentiostat (PAR, Versa state IV), both in the dark and under front side illumination, using a Xe lamp (150 W, Oriel) with an AM 1.5 filter. Potentials with respect to the reversible hydrogen electrode (RHE) scale (E_{RHE}) were calculated using the Nernst equation:[32]

$$E_{RHE} = E_{SCE} + E^0_{SCE} + 0.059\ pH \quad (1)$$

where E_{SCE} and E^0_{SCE} are the actual and standard potentials against SCE.

STH values are calculated basing of the following equation:[5,31]

$$\text{STH efficiency } (\%) = j \times (1.23 - E_{RHE}) / I_{light} \quad (2)$$

where E_{RHE} is the applied bias *vs.* RHE and I_{light} denotes the irradiance intensity (equal to 100 mW/cm^2 for AM 1.5G illumination).

TAS experiments were performed on photoanodes having a geometric area of 3×3 cm^2 in a three-electrode PEC cell (Zahner-elektrik PECC-2) with a Pt counter-electrode, an Ag/AgCl (3 M KCl) reference electrode, and 0.1 M NaOH electrolyte (degassed with N_2 prior to

measurements). A potential value of 1.6 V *vs*. RHE was controlled by a standard potentiostat (CompactStat, Ivium Technologies) to probe the charge dynamics under water splitting conditions. TAS measurements in a microsecond-to-second timescale were carried out by a modified flash-photolysis apparatus (Luzchem LFP-111) with a New Focus (model 2051) photodetector and a halogen lamp (9 W, Thorlabs SLS201/M) probe. The excitation was fixed at λ = 355 nm, with an energy density of 0.4 mJ/cm^2. The transient absorption traces were averaged 50–80 times.

The picosecond-to-nanosecond TAS experiments were performed by a pump-probe system consisting of Libra F-1K (Coherent Inc.) generator producing 100 fs pulses at λ = 800 nm (1 mJ) with a repetition rate of 1 kHz.[70] An optical parametric amplifier (Topas-C, Light Conversion Ltd.) was used to provide pump pulses at λ = 355 nm. The measuring component was ExciPro (CDP Inc.) equipped with two array photodetectors coupled with a spectrometer (CDP2022i) set for probe detection in the 500–700 nm interval, with averaging over 10000 excitation shots. The maximum time range available for probing was ≈ 6 ns. TAS decays were fitted by using exponential functions in oder to eluciate the charge transfer processes and corresponding timescales in the studied photoanode systems.

Supporting Information

Supporting Information is available from the Wiley Online Library or from the author.

Acknowledgements

The authors kindly acknowledge the financial support under the FP7 project "SOLAROGENIX" (NMP4-SL-2012-310333), as well as Padova University ex-60% 2012-2014 projects, grant n°CPDR132937/13 (SOLLEONE), and Regione Lombardia-INSTM ATLANTE projects. S.T. acknowledges the FWO Flanders for a post-doctoral scholarship.

References

(1) Moniz, S. J. A.; Shevlin, S. A.; Martin, D. J.; Guo, Z.-X.; Tang, J. Visible-light driven heterojunction photocatalysts for water splitting - a critical review. *Energy Environ. Sci.* **2015**, *8*, 731-759.

(2) Liu, R.; Zheng, Z.; Spurgeon, J.; Yang, X. Enhanced photoelectrochemical water-splitting performance of semiconductors by surface passivation layers. *Energy Environ. Sci.* **2014**, *7*, 2504-2517.

(3) Hung, W. H.; Chien, T. M.; Lo, A. Y.; Tseng, C. M.; Li, D. D. Spatially controllable plasmon enhanced water splitting photocurrent in Au/TiO2-Fe2O3 cocatalyst system. *Rsc Adv*. **2014**, *4*, 45710-45714.

(4) Luan, P.; Xie, M.; Fu, X.; Qu, Y.; Sun, X.; Jing, L. Improved photoactivity of TiO2-Fe2O3 nanocomposites for visible-light water splitting after phosphate bridging and its mechanism. *Phys. Chem. Chem. Phys.* **2015**, *17*, 5043-5050.

(5) Hernández, S.; Cauda, V.; Hidalgo, D.; Farías Rivera, V.; Manfredi, D.; Chiodoni, A.; Pirri, F. C. Fast and low-cost synthesis of 1D ZnO–TiO2 core–shell nanoarrays: Characterization and enhanced photo-electrochemical performance for water splitting. *J. All. Compnd.* **2014**, *615, Supplement 1*, S530-S537.

(6) Yang, X.; Liu, R.; Du, C.; Dai, P.; Zheng, Z.; Wang, D. Improving Hematite-based Photoelectrochemical Water Splitting with Ultrathin TiO2 by Atomic Layer Deposition. *ACS Appl. Mater. Interf.* **2014**, *6*, 12005-12011.

(7) Rioult, M.; Magnan, H.; Stanescu, D.; Barbier, A. Single Crystalline Hematite Films for Solar Water Splitting: Ti-Doping and Thickness Effects. *J. Phys. Chem. C* **2014**, *118*, 3007-3014.

(8) Barreca, D.; Carraro, G.; Gombac, V.; Gasparotto, A.; Maccato, C.; Fornasiero, P.; Tondello, E. Supported Metal Oxide Nanosystems for Hydrogen Photogeneration: Quo Vadis? *Adv. Funct. Mater.* **2011**, *21*, 2611-2623.

(9) Carraro, G.; Maccato, C.; Gasparotto, A.; Montini, T.; Turner, S.; Lebedev, O. I.; Gombac, V.; Adami, G.; Van Tendeloo, G.; Barreca, D.; Fornasiero, P. Enhanced Hydrogen Production by Photoreforming of Renewable Oxygenates Through Nanostructured Fe2O3 Polymorphs. *Adv. Funct. Mater.* **2014**, *24*, 372-378.

(10) Cao, D. P.; Luo, W. J.; Feng, J. Y.; Zhao, X.; Li, Z. S.; Zou, Z. G. Cathodic shift of onset potential for water oxidation on a Ti4+ doped Fe2O3 photoanode by suppressing the back reaction. *Energy Environ. Sci.* **2014**, *7*, 752-759.

(11) Mor, G. K.; Prakasam, H. E.; Varghese, O. K.; Shankar, K.; Grimes, C. A. Vertically oriented Ti-Fe-O nanotube array films: Toward a useful material architecture for solar spectrum water photoelectrolysis. *Nano Lett.* **2007**, *7*, 2356-2364.

(12) Wang, L.; Lee, C. Y.; Schmuki, P. Ti and Sn co-doped anodic alpha-Fe2O3 films for efficient water splitting. *Electrochem. Comm.* **2013**, *30*, 21-25.

(13) Lian, X. J.; Yang, X.; Liu, S. J.; Xu, Y.; Jiang, C. P.; Chen, J. W.; Wang, R. L. Enhanced photoelectrochemical performance of Ti-doped hematite thin films prepared by the sol-gel method. *Appl. Surf. Sci.* **2012**, *258*, 2307-2311.

(14) Kronawitter, C. X.; Ma, Z.; Liu, D.; Mao, S. S.; Antoun, B. R. Engineering Impurity Distributions in Photoelectrodes for Solar Water Oxidation. *Adv. Energy Mater.* **2012**, *2*, 52-57.

(15) Kim, J. H.; Kim, J. H.; Jang, J.-W.; Kim, J. Y.; Choi, S. H.; Magesh, G.; Lee, J.; Lee, J. S. Awakening Solar Water-Splitting Activity of ZnFe2O4 Nanorods by Hybrid Microwave Annealing. *Adv. Energy Mater.* **2014**, n/a-n/a.

(16) Luan, P.; Xie, M.; Liu, D.; Fu, X.; Jing, L. Effective charge separation in the rutile TiO2 nanorod-coupled α-Fe2O3 with exceptionally high visible activities. *Sci. Rep.* **2014**, *4*, 6180.

(17) Zandi, O.; Klahr, B. M.; Hamann, T. W. Highly photoactive Ti-doped alpha-Fe2O3 thin film electrodes: resurrection of the dead layer. *Energy Environ. Sci.* **2013**, *6*, 634-642.

(18) Zhang, P.; Kleiman-Shwarsctein, A.; Hu, Y. S.; Lefton, J.; Sharma, S.; Forman, A. J.; McFarland, E. Oriented Ti doped hematite thin film as active photoanodes synthesized by facile APCVD. *Energy Environ. Sci.* **2011**, *4*, 1020-1028.

(19) Klahr, B.; Gimenez, S.; Fabregat-Santiago, F.; Hamann, T.; Bisquert, J. Water Oxidation at Hematite Photoelectrodes: The Role of Surface States. *J. Am. Chem. Soc.* **2012**, *134*, 4294-4302.

(20) Le Formal, F.; Tetreault, N.; Cornuz, M.; Moehl, T.; Gratzel, M.; Sivula, K. Passivating surface states on water splitting hematite photoanodes with alumina overlayers. *Chem. Sci.* **2011**, *2*, 737-743.

(21) Steier, L.; Herraiz-Cardona, I.; Gimenez, S.; Fabregat-Santiago, F.; Bisquert, J.; Tilley, S. D.; Grätzel, M. Understanding the Role of Underlayers and Overlayers in Thin Film Hematite Photoanodes. *Adv. Funct. Mater.* **2014**, *24*, 7681-7688.

(22) Magnan, H.; Stanescu, D.; Rioult, M.; Fonda, E.; Barbier, A. Enhanced photoanode properties of epitaxial Ti doped alpha-Fe2O3 (0001) thin films. *Appl. Phys. Lett.* **2012**, *101*, 133908.

(23) Li, S.; Zhang, P.; Song, X.; Gao, L. Ultrathin Ti-doped hematite photoanode by pyrolysis of ferrocene. *Int. J. Hydrogen Energy* **2014**, *39*, 14596-14603.

(24) Wheeler, D. A.; Wang, G.; Ling, Y.; Li, Y.; Zhang, J. Z. Nanostructured Hematite: Synthesis, Characterization, Charge Carrier Dynamics, and Photoelectrochemical Properties. *Energy Environ. Sci.* **2012**, *5*, 6682-6702.

(25) Carroll, G. M.; Zhong, D. K.; Gamelin, D. R. Mechanistic insights into solar water oxidation by cobalt-phosphate-modified [small alpha]-Fe2O3 photoanodes. *Energy Environ. Sci.* **2015**, *8*, 577-584.

(26) Hung, W.-H.; Chien, T.-M.; Tseng, C.-M. Enhanced Photocatalytic Water Splitting by Plasmonic TiO2–Fe2O3 Cocatalyst under Visible Light Irradiation. *J. Phys. Chem. C* **2014**, *118*, 12676-12681.

(27) Wang, D.; Zhang, X.-T.; Sun, P.-P.; Lu, S.; Wang, L.-L.; Wei, Y.-A.; Liu, Y.-C. Enhanced photoelectrochemical water splitting on hematite thin film with layer-by-layer deposited ultrathin TiO2 underlayer. *Int. J. Hydrogen Energy* **2014**, *39*, 16212-16219.

(28) Zhang, C.; Wu, Q.; Ke, X.; Wang, J.; Jin, X.; Xue, S. Ultrathin hematite films deposited layer-by-layer on a TiO2 underlayer for efficient water splitting under visible light. *Int. J. Hydrogen Energy* **2014**, *39*, 14604-14612.

(29) Li, Z.; Luo, W.; Zhang, M.; Feng, J.; Zou, Z. Photoelectrochemical cells for solar hydrogen production: current state of promising photoelectrodes, methods to improve their properties, and outlook. *Energy Environ. Sci.* **2013**, *6*, 347-370.

(30) Lin, Y.; Zhou, S.; Sheehan, S. W.; Wang, D. Nanonet-Based Hematite Heteronanostructures for Efficient Solar Water Splitting. *J. Am. Chem. Soc.* **2011**, *133*, 2398-2401.

(31) Sharma, P.; Kumar, P.; Deva, D.; Shrivastav, R.; Dass, S.; Satsangi, V. R. Nanostructured Zn-Fe2O3 thin film modified by Fe-TiO2 for photoelectrochemical generation of hydrogen. *Int. J. Hydrogen Energy* **2010**, *35*, 10883-10889.

(32) Wang, G.; Ling, Y.; Wheeler, D. A.; George, K. E. N.; Horsley, K.; Heske, C.; Zhang, J. Z.; Li, Y. Facile Synthesis of Highly Photoactive alpha-Fe2O3-Based Films for Water Oxidation. *Nano Lett.* **2011**, *11*, 3503-3509.

(33) Hahn, N. T.; Mullins, C. B. Photoelectrochemical Performance of Nanostructured Ti- and Sn-Doped alpha-Fe2O3 Photoanodes. *Chem. Mater.* **2010**, *22*, 6474-6482.

(34) Mirbagheri, N.; Wang, D.; Peng, C.; Wang, J.; Huang, Q.; Fan, C.; Ferapontova, E. E. Visible Light Driven Photoelectrochemical Water Oxidation by Zn- and Ti-Doped Hematite Nanostructures. *ACS Catal.* **2014**, *4*, 2006-2015.

(35) Zhong, D. K.; Cornuz, M.; Sivula, K.; Gratzel, M.; Gamelin, D. R. Photo-assisted electrodeposition of cobalt-phosphate (Co-Pi) catalyst on hematite photoanodes for solar water oxidation. *Energy Environ. Sci.* **2011**, *4*, 1759-1764.

(36) Fu, Z.; Jiang, T.; Liu, Z.; Wang, D.; Wang, L.; Xie, T. Highly photoactive Ti-doped α-Fe2O3 nanorod arrays photoanode prepared by a hydrothermal method for photoelectrochemical water splitting. *Electrochim. Acta* **2014**, *129*, 358-363.

(37) Xi, L.; Chiam, S. Y.; Mak, W. F.; Tran, P. D.; Barber, J.; Loo, S. C. J.; Wong, L. H. A novel strategy for surface treatment on hematite photoanode for efficient water oxidation. *Chem. Sci.* **2013**, *4*, 164-169.

(38) Lee, M. H.; Park, J. H.; Han, H. S.; Song, H. J.; Cho, I. S.; Noh, J. H.; Hong, K. S. Nanostructured Ti-doped hematite (alpha-Fe2O3) photoanodes for efficient photoelectrochemical water oxidation. *Int. J. Hydrogen Energy* **2014**, *39*, 17501-17507.

(39) Deng, J. J.; Zhong, J.; Pu, A. W.; Zhang, D.; Li, M.; Sun, X. H.; Lee, S. T. Ti-doped hematite nanostructures for solar water splitting with high efficiency. *J. Appl. Phys.* **2012**, *112*, 084312.

(40) Barreca, D.; Carraro, G.; Gasparotto, A.; Maccato, C.; Sada, C.; Singh, A. P.; Mathur, S.; Mettenbörger, A.; Bontempi, E.; Depero, L. E. Columnar Fe_2O_3 Arrays via Plasma-enhanced Growth: Interplay of Fluorine Substitution and Photoelectrochemical Properties. *Int. J. Hydrogen Energy* **2013**, *38*, 14189-14199.

(41) Kronawitter, C. X.; Zegkinoglou, I.; Shen, S. H.; Liao, P.; Cho, I. S.; Zandi, O.; Liu, Y. S.; Lashgari, K.; Westin, G.; Guo, J. H.; Himpsel, F. J.; Carter, E. A.; Zheng, X. L.; Hamann, T. W.; Koel, B. E.; Mao, S. S.; Vayssieres, L. Titanium incorporation into

hematite photoelectrodes: theoretical considerations and experimental observations. *Energy Environ. Sci.* **2014**, *7*, 3100-3121.

(42) Shen, S.; Kronawitter, C. X.; Wheeler, D. A.; Guo, P.; Lindley, S. A.; Jiang, J.; Zhang, J. Z.; Guo, L.; Mao, S. S. Physical and photoelectrochemical characterization of Ti-doped hematite photoanodes prepared by solution growth. *J. Mater. Chem. A* **2013**, *1*, 14498-14506.

(43) Miao, C. H.; Shi, T. F.; Xu, G. P.; Ji, S. L.; Ye, C. H. Photocurrent Enhancement for Ti-Doped Fe2O3 Thin Film Photoanodes by an In Situ Solid-State Reaction Method. *Acs Appl. Mater. Interf.* **2013**, *5*, 1310-1316.

(44) Moniz, S. J. A.; Shevlin, S. A.; An, X.; Guo, Z.-X.; Tang, J. Fe2O3–TiO2 Nanocomposites for Enhanced Charge Separation and Photocatalytic Activity. *Chem. – A Eur. J.* **2014**, *20*, 15571-15579.

(45) Mayer, M. T.; Lin, Y.; Yuan, G.; Wang, D. Forming Heterojunctions at the Nanoscale for Improved Photoelectrochemical Water Splitting by Semiconductor Materials: Case Studies on Hematite. *Acc. Chem. Res.* **2013**, *46*, 1558-1566.

(46) Kronawitter, C. X.; Vayssieres, L.; Shen, S.; Guo, L.; Wheeler, D. A.; Zhang, J. Z.; Antoun, B. R.; Mao, S. S. A perspective on solar-driven water splitting with all-oxide hetero-nanostructures. *Energy Environ. Sci.* **2011**, *4*, 3889-3899.

(47) Kim, J. Y.; Magesh, G.; Youn, D. H.; Jang, J.-W.; Kubota, J.; Domen, K.; Lee, J. S. Single-crystalline, Wormlike Hematite Photoanodes for Efficient Solar Water Splitting. *Sci. Rep.* **2013**, *3*, 2681.

(48) Barreca, D.; Carraro, G.; Gasparotto, A.; Maccato, C.; Rossi, F.; Salviati, G.; Tallarida, M.; Das, C.; Fresno, F.; Korte, D.; Stangar, U. L.; Franko, M.; Schmeisser, D. Surface Functionalization of Nanostructured Fe_2O_3 Polymorphs: From Design to Light-Activated Applications. *Acs Appl. Mater. Interf.* **2013**, *5*, 7130-7138.

(49) Kumari, S.; Singh, A. P.; Sonal; Deva, D.; Shrivastav, R.; Dass, S.; Satsangi, V. R. Spray pyrolytically deposited nanoporous Ti4+ doped hematite thin films for efficient photoelectrochemical splitting of water. *Int. J. Hydrogen Energy* **2010**, *35*, 3985-3990.

(50) Ling, Y.; Wang, G.; Wheeler, D. A.; Zhang, J. Z.; Li, Y. Sn-Doped Hematite Nanostructures for Photoelectrochemical Water Splitting. *Nano Lett.* **2011**, *11*, 2119-2125.

(51) Warwick, M. E. A.; Kaunisto, K.; Barreca, D.; Carraro, G.; Gasparotto, A.; Maccato, C.; Bontempi, E.; Sada, C.; Ruoko, T.-P.; Turner, S.; Van Tendeloo, G. Vapor phase processing of α-Fe2O3 photoelectrodes for water splitting: an insight into the structure/property interplay. *ACS Applied Materials & Interfaces* **2015**.

(52) Luo, J.; Xia, X.; Luo, Y.; Guan, C.; Liu, J.; Qi, X.; Ng, C. F.; Yu, T.; Zhang, H.; Fan, H. J. Rationally Designed Hierarchical TiO2@Fe2O3 Hollow Nanostructures for Improved Lithium Ion Storage. *Adv. Energy Mater.* **2013**, *3*, 737-743.

(53) Pattern N° 33-0664, JCPDS (2000).

(54) Pattern N° 00-021-1272, JCPDS (2000).

(55) Ji, S. M.; Jun, H.; Jang, J. S.; Son, H. C.; Borse, P. H.; Lee, J. S. Photocatalytic hydrogen production from natural seawater. *J. Photochem. Photobiol. A* **2007**, *189*, 141-144.

(56) Joo, H.; Bae, S.; Kim, C.; Kim, S.; Yoon, J. Hydrogen evolution in enzymatic photoelectrochemical cell using modified seawater electrolytes produced by membrane desalination process. *Solar Energy Mater. Solar Cells* **2009**, *93*, 1555-1561.

(57) Augustynski, J.; Solarska, R.; Hagemann, H.; Santato, C. In *Nanostructured thin-film tungsten trioxide photoanodes for solar water and sea-water splitting*, 2006; pp 63400J-63400J-63409.

(58) Barroso, M.; Pendlebury, S. R.; Cowan, A. J.; Durrant, J. R. Charge carrier trapping, recombination and transfer in hematite ([small alpha]-Fe2O3) water splitting photoanodes. *Chem. Sci.* **2013**, *4*, 2724-2734.

(59) Pendlebury, S. R.; Wang, X.; Le Formal, F.; Cornuz, M.; Kafizas, A.; Tilley, S. D.; Grätzel, M.; Durrant, J. R. Ultrafast Charge Carrier Recombination and Trapping in Hematite Photoanodes under Applied Bias. *J. Am. Chem. Soc.* **2014**, *136*, 9854-9857.

(60) Fitzmorris, B. C.; Patete, J. M.; Smith, J.; Mascorro, X.; Adams, S.; Wong, S. S.; Zhang, J. Z. Ultrafast Transient Absorption Studies of Hematite Nanoparticles: The Effect of Particle Shape on Exciton Dynamics. *ChemSusChem* **2013**, *6*, 1907-1914.

(61) Cowan, A. J.; Leng, W.; Barnes, P. R. F.; Klug, D. R.; Durrant, J. R. Charge Carrier Separation in Nanostructured TiO_2 Photoelectrodes for Water Splitting. *Phys. Chem. Chem. Phys.* **2013**, *15*, 8772-8778.

(62) Tang, J.; Durrant, J. R.; Klug, D. R. Mechanism of Photocatalytic Water Splitting in TiO2. Reaction of Water with Photoholes, Importance of Charge Carrier Dynamics, and Evidence for Four-Hole Chemistry. *J. Am. Chem. Soc.* **2008**, *130*, 13885-13891.

(63) Cowan, A. J.; Barnett, C. J.; Pendlebury, S. R.; Barroso, M.; Sivula, K.; Grätzel, M.; Durrant, J. R.; Klug, D. R. Activation Energies for the Rate-Limiting Step in Water Photooxidation by Nanostructured α-Fe2O3 and TiO2. *J. Am. Chem. Soc.* **2011**, *133*, 10134-10140.

(64) Tang, J.; Cowan, A. J.; Durrant, J. R.; Klug, D. R. Mechanism of O2 Production from Water Splitting: Nature of Charge Carriers in Nitrogen Doped Nanocrystalline TiO2 Films and Factors Limiting O2 Production. *J. Phys. Chem. C* **2011**, *115*, 3143-3150.

(65) Baxter, J. B.; Richter, C.; Schmuttenmaer, C. A. Ultrafast Carrier Dynamics in Nanostructures for Solar Fuels. *An. Rev. Phys. Chem.* **2014**, *65*, 423-447.

(66) Peng, L.; Xie, T.; Lu, Y.; Fan, H.; Wang, D. Synthesis, photoelectric properties and photocatalytic activity of the Fe2O3/TiO2 heterogeneous photocatalysts. *Phys. Chem. Chem. Phys.* **2010**, *12*, 8033-8041.

(67) Carraro, G.; Gasparotto, A.; Maccato, C.; Bontempi, E.; Bilo, F.; Peeters, D.; Sada, C.; Barreca, D. A plasma-assisted approach for the controlled dispersion of CuO aggregates into [small beta] iron(iii) oxide matrices. *CrystEngComm* **2014**, *16*, 8710-8716.

(68) Barreca, D.; Carraro, G.; Devi, A.; Fois, E.; Gasparotto, A.; Seraglia, R.; Maccato, C.; Sada, C.; Tabacchi, G.; Tondello, E.; Venzo, A.; Winter, M. β-Fe2O3 nanomaterials from an iron(ii) diketonate-diamine complex: a study from molecular precursor to growth process. *Dalton Trans.* **2012**, *41*, 149-155.

(69) Briggs, D.; Seah, M. P., *Practical Surface Analysis: Auger and X-ray Photoelectron Spectroscopy*. John Wiley & Sons: New York, 2nd ed.: 1990.

(70) Sirbu, D.; Turta, C.; Benniston, A. C.; Abou-Chahine, F.; Lemmetyinen, H.; Tkachenko, N. V.; Wood, C.; Gibson, E. Synthesis and properties of a meso- tris-ferrocene appended zinc(ii) porphyrin and a critical evaluation of its dye sensitised solar cell (DSSC) performance. *RSC Adv*. **2014**, *4*, 22733-22742.

Sample ID	Fe_2O_3 by PE-CVD	TiO_2 by ALD	Thermal Anneling
Fe_2O_3	400°C, 1 h	//	
400_L	400°C, 1 h	150°C, 1150 cycles	650°C, 1 h, air
400_H	400°C, 1 h	150°C, 5750 cycles	

Table 1. Main growth and processing conditions for FTO-supported photoanodes investigated in the present study.

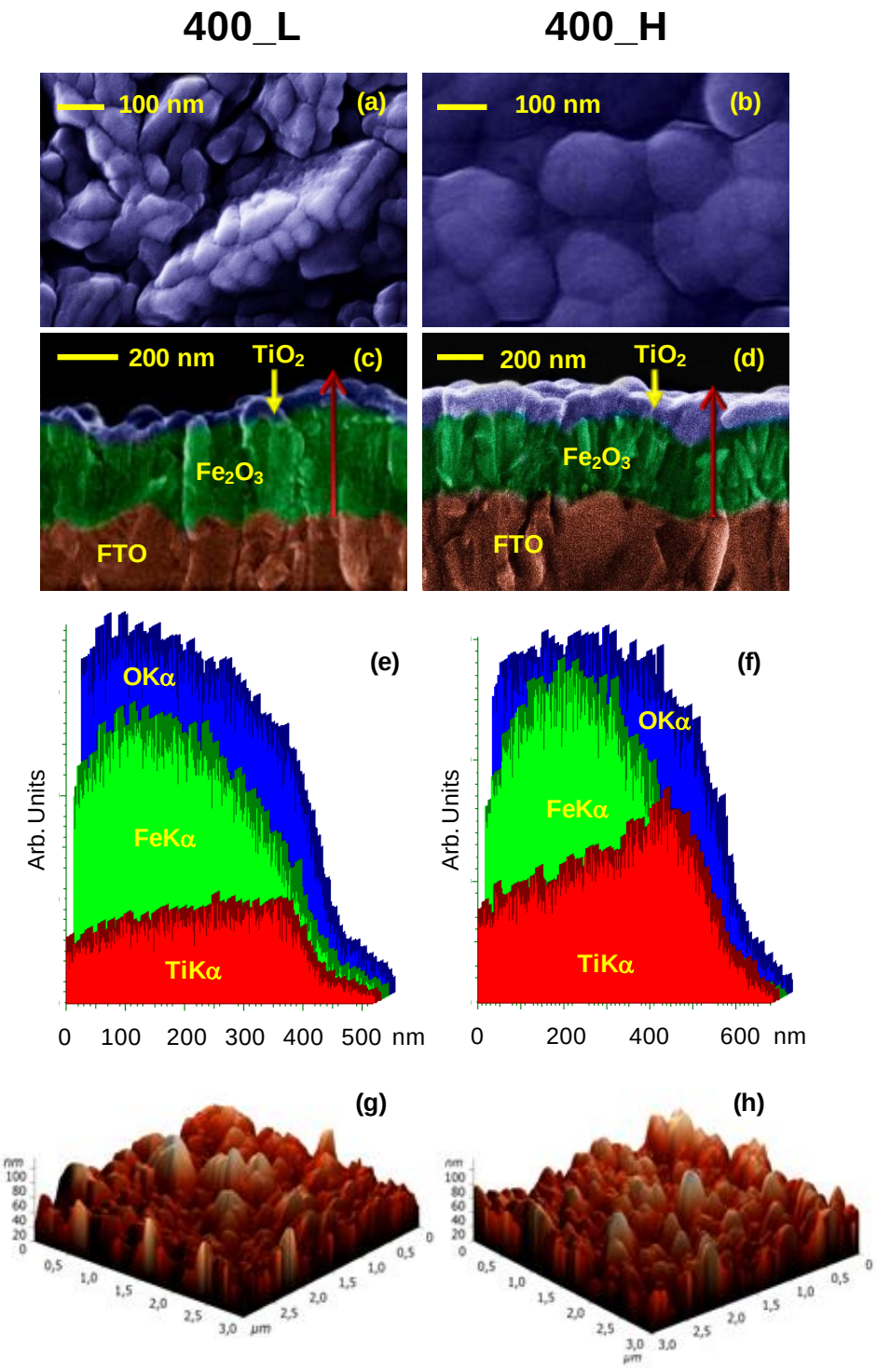

Figure 1. (a,b) Plane-view FE-SEM images, (c,d) cross-sectional FE-SEM images, (e,f) EDXS line-scan profiles recorded along the lines marked in cross-sectional views, and (g,h) AFM micrographs for Fe_2O_3-TiO_2 specimens. In (e) and (f), arrows mark the direction of abscissa increase.

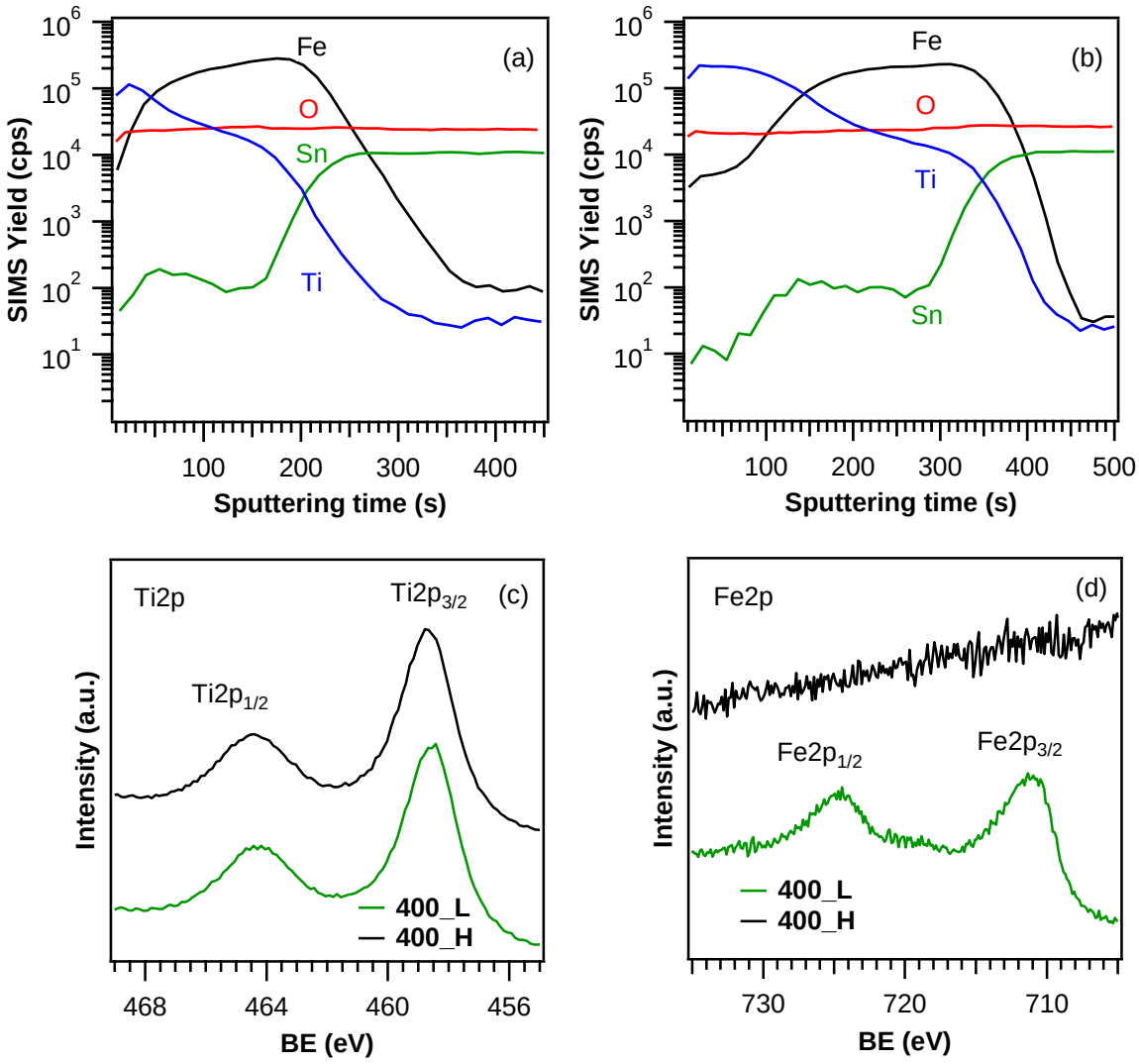

Figure 2. SIMS depth profiles for Fe_2O_3-TiO_2 deposits on FTO: (a) **400_L**; (b) **400_H**. (c) Ti2p, and (d) Fe2p XPS surface spectra for the same systems.

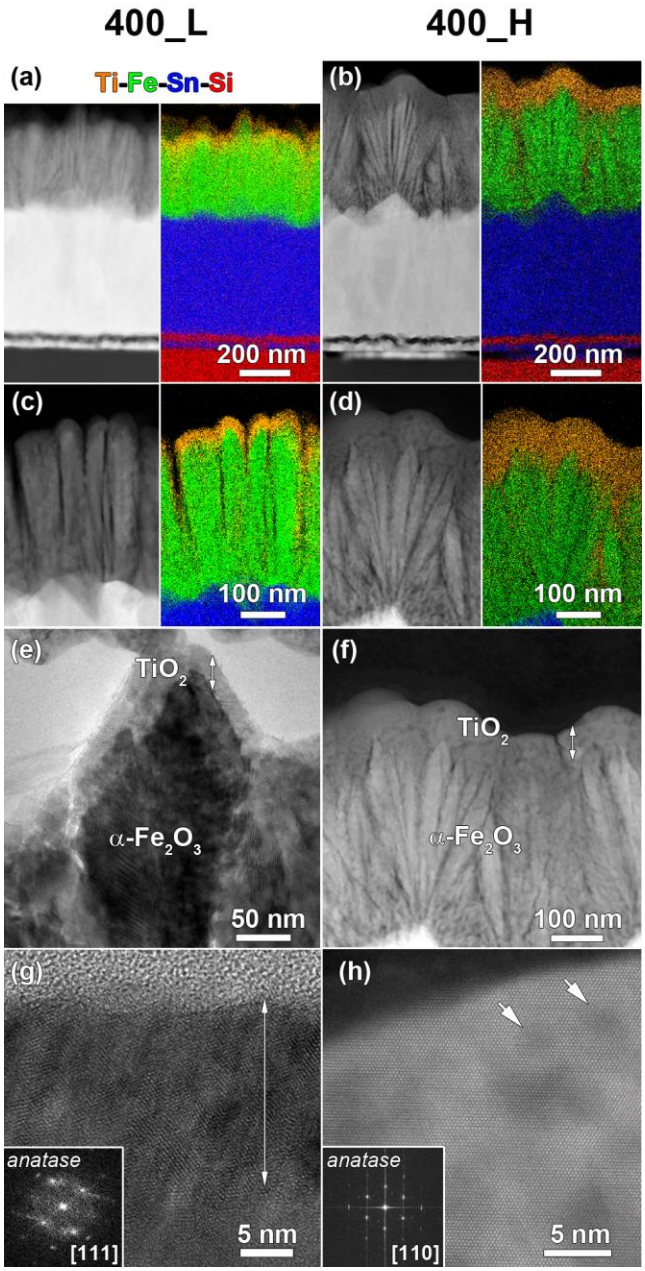

Figure 3. TEM characterization of Fe_2O_3-TiO_2 photoanodes. (a-d) Cross sectional HAADF-STEM images and corresponding EDXS chemical maps of samples **400_L** (a,c) and **400_H** (b,d). (e) TEM overview image of sample **400_L**. (f) HAADF-STEM overview of sample **400_H**. ~~In both cases, the TiO_2 overlayer thickness is marked by a double-ended arrow.~~ (g) HR-TEM image of sample **400_L**, evidencing the low crystallinity of the *anatase* top layer. The *anatase* layer is imaged along the [111] zone axis, as evidenced by the inset Fourier Transform (FT) pattern. In (e,f,g), the TiO_2 overlayer thickness is marked by a double-ended arrow. (h) High resolution HAADF-STEM image of sample **400_H**, with arrows indicating the presence of small dark-contrast voids in the highly crystalline *anatase* overlayer. The *anatase* layer is imaged along the [110] zone axis, as evidenced by the inset FT pattern.

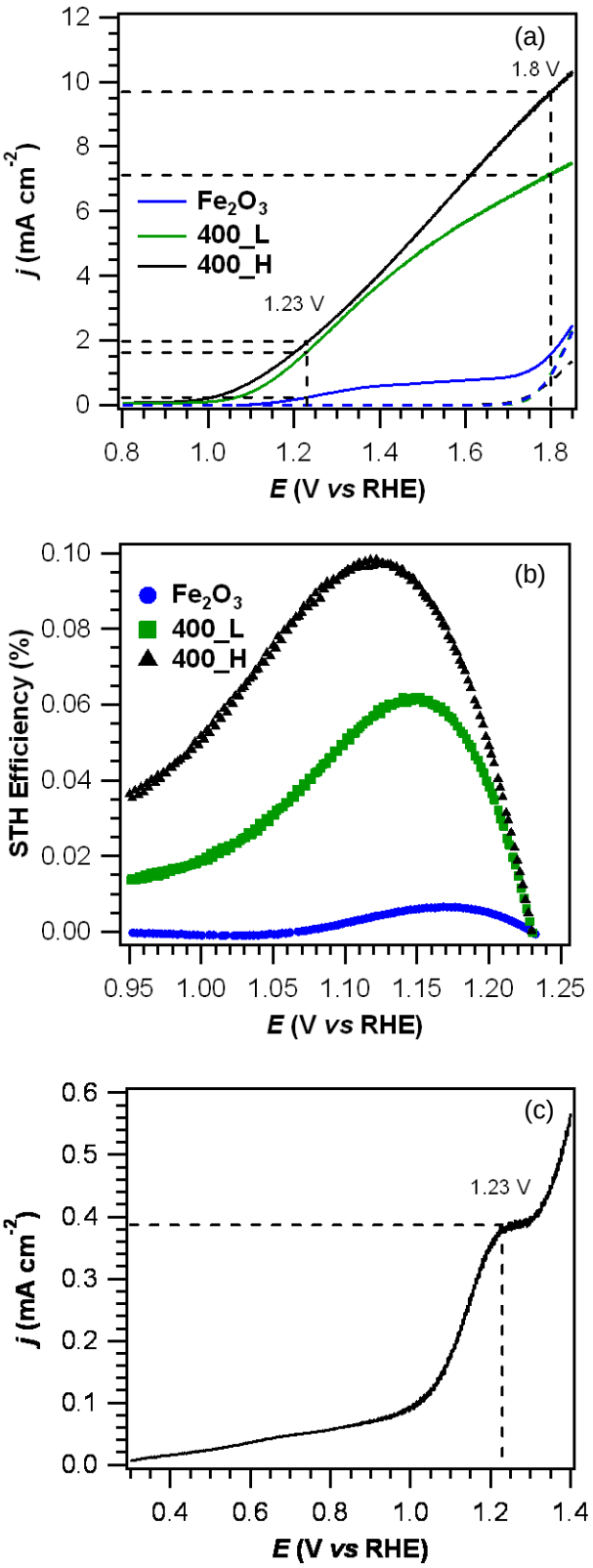

Figure 4. (a) Photocurrent density against applied potential curves for Fe_2O_3 and Fe_2O_3-TiO_2 photoelectrodes recorded in NaOH solution (pH = 13.6) under simulated solar light irradiation (continuous lines) and in the dark (dashed lines). (b) Calculated solar-to-hydrogen (STH)

efficiencies. (c) *j*-V curve for specimen **400_H** in a simulated seawater solution under solar irradiation.

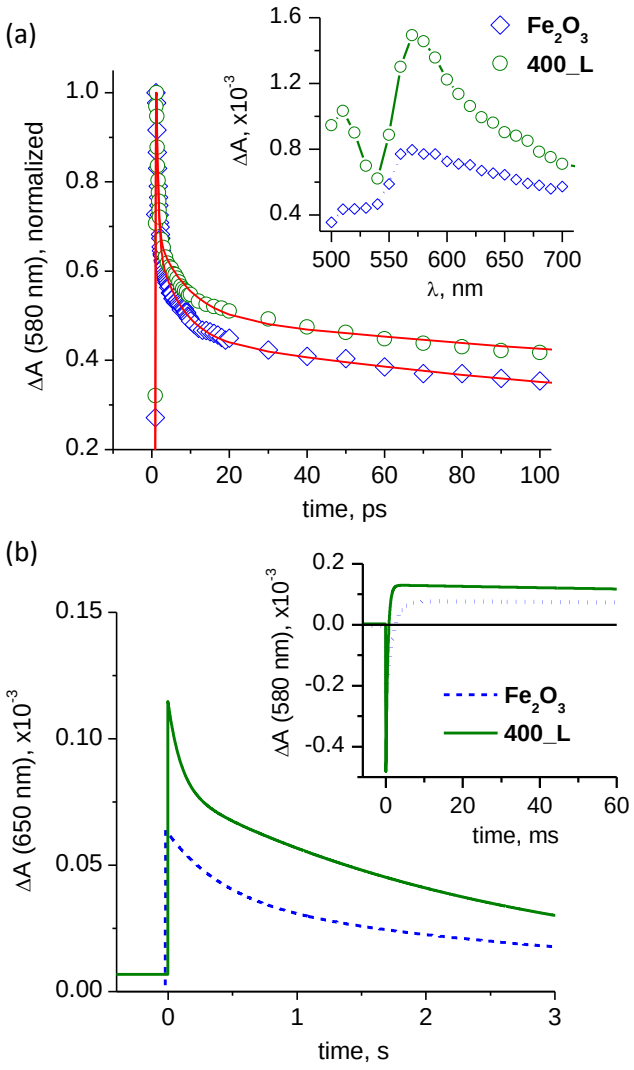

Figure 5. (a) Normalized ultrafast TAS decays for Fe_2O_3 and Fe_2O_3-TiO_2 (**400_L**) photoelectrodes. The red lines show 4-exponential fits of raw data. The inset presents the corresponding longest-lived component spectra with lifetimes exceeding the 6 ns delay. (b) Bi-exponential fits of the TAS decays for Fe_2O_3 and Fe_2O_3-TiO_2 (**400_L**) specimens on a second timescale. The corresponding bi-exponential fits of TAS decays in a millisecond time range are shown in the inset.

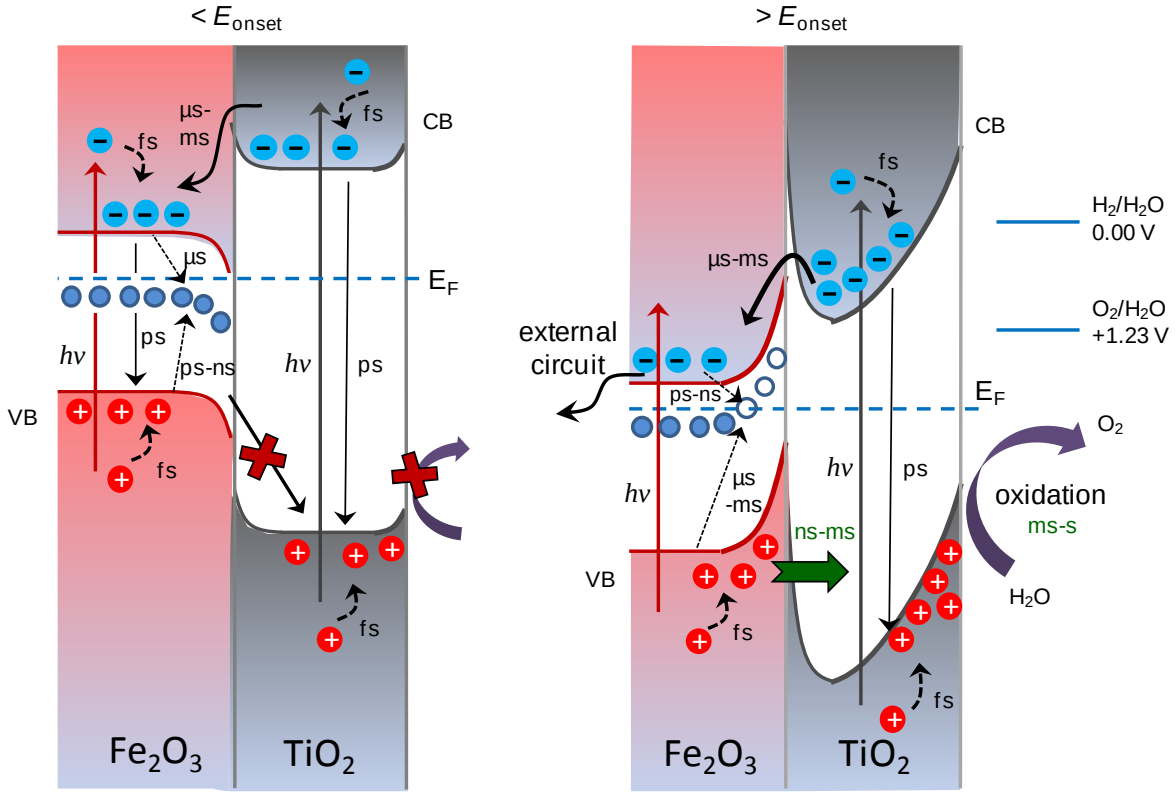

Scheme 1. Schematic energy level diagrams illustrating the photo-activated charge transfer processes and related timescales under low (left) and high (right) positive external bias in the TiO_2-Fe_2O_3 photoanodes. The intra-band electron trap states, located a few 100 mV below the conduction band edge of *hematite*, are also shown. (CB: conduction band, VB: valence band, E_F: Fermi level, fs: femtosecond, ps: picosecond, ns: nanosecond, μs: microsecond, ms: millisecond).

Table of contents entry

Keywords: Fe_2O_3; TiO_2; nano-heterostructures; water splitting; PEC.

Fe_2O_3-TiO_2 nano-heterostructure photoanodes for highly efficient solar water oxidation

M.E.A. Warwick, G. Carraro, C. Maccato, A. Gasparotto, K. Kaunisto, C. Sada, S. Turner, Y. Gönüllü, T.-P. Ruoko, L. Borgese, E. Bontempi, G. Van Tendeloo, H. Lemmetyinen, S. Mathur, and D. Barreca*

Fe_2O_3-TiO_2 photoanodes for photoelectrochemical water splitting were fabricated on FTO substrates by a two-step vapor-phase synthetic strategy, followed by thermal annealing in air. The record-breaking performances of ≈10.0 mA/cm^2 photocurrent at 1.8 V *vs.* RHE under simulated solar irradiation, along with the system activity even in seawater, provide a key milestone for the sustainable generation of renewable energy starting from abundant natural resources.

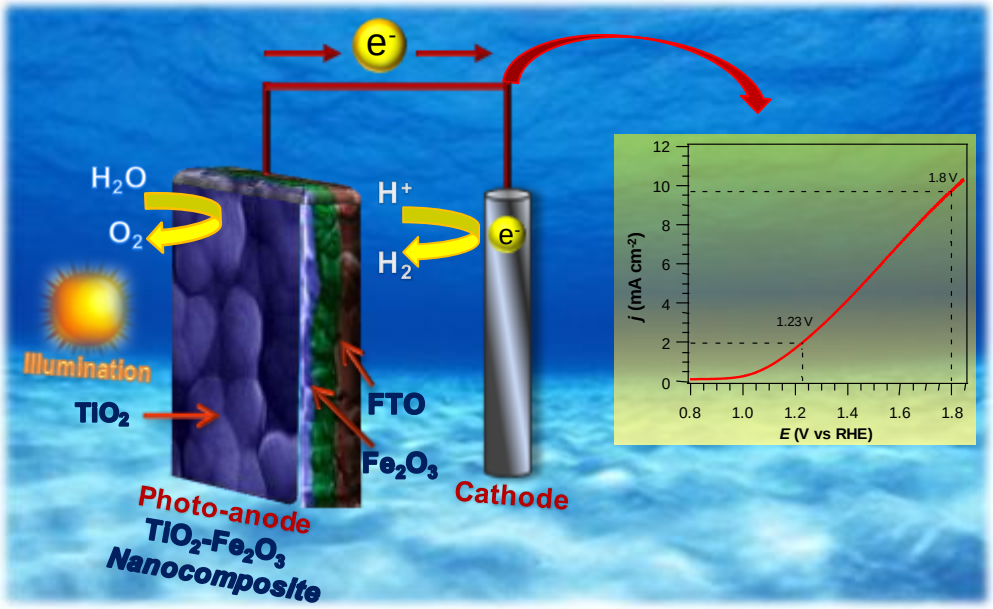

Supporting Information

Fe_2O_3-TiO_2 nano-heterostructure photoanodes for highly efficient solar water oxidation

By *Michael E.A. Warwick, Giorgio Carraro, Chiara Maccato, Alberto Gasparotto, Kimmo Kaunisto, Cinzia Sada, Stuart Turner, Yakup Gönüllü, Tero-Petri Ruoko, Laura Borgese, Elza Bontempi, Gustaaf Van Tendeloo, Helge Lemmetyinen, Sanjay Mathur and Davide Barreca**

Dr. M.E.A. Warwick, Dr. G. Carraro, Prof. C. Maccato, Dr. A. Gasparotto
Department of Chemistry, Padova University and INSTM, 35131 Padova, Italy.

Dr. K. Kaunisto, Mr. T.-P. Ruoko, Prof. H. Lemmetyinen
Department of Chemistry and Bioengineering, Tampere University of Technology, 33101 Tampere, Finland.

Prof. C. Sada
Department of Physics and Astronomy, Padova University, 35131 Padova, Italy.

Dr. S. Turner, Prof. G. Van Tendeloo
EMAT, University of Antwerp, 2020 Antwerpen, Belgium.

Dr. Y. Gönüllü, Prof. S. Mathur
Department of Chemistry, Chair of Inorganic and Materials Chemistry, Cologne University, 50939 Cologne, Germany.

Dr. L. Borgese, Prof. E. Bontempi
Chemistry for Technologies Laboratory, Brescia University, 25123 Brescia, Italy.

[*] Dr. D. Barreca
CNR-IENI and INSTM - Department of Chemistry, Padova University, 35131 Padova, Italy.
E-mail: davide.barreca@unipd.it

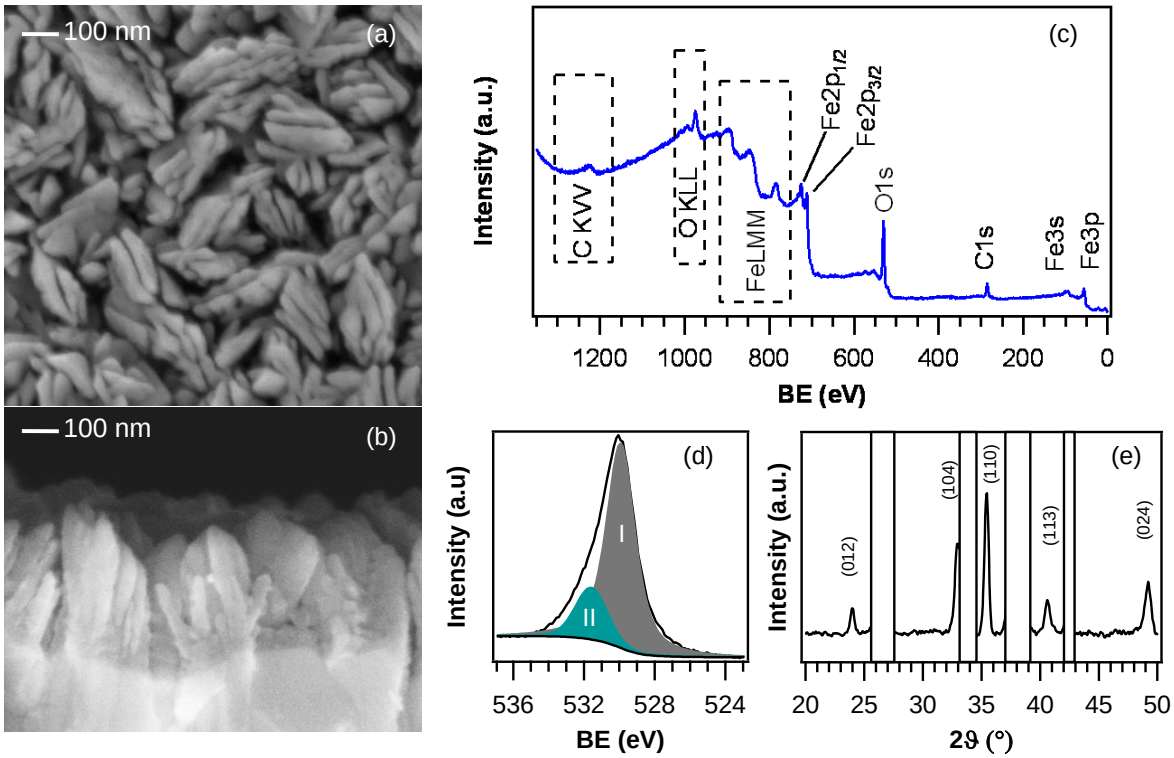

Figure S1. Charaterization of bare Fe_2O_3 photoelectrodes supported on FTO. (a,b) Plane-view and cross-sectional FE-SEM micrographs; (c) surface XPS wide-scan spectrum and (d) O1s photopeak; (e) XRD pattern. In the latter case, reflections pertaining to the FTO-coated glass substrate have been covered for clarity. All the indexed peaks correspond to α-Fe_2O_3 (*hematite*) reflections.[53]

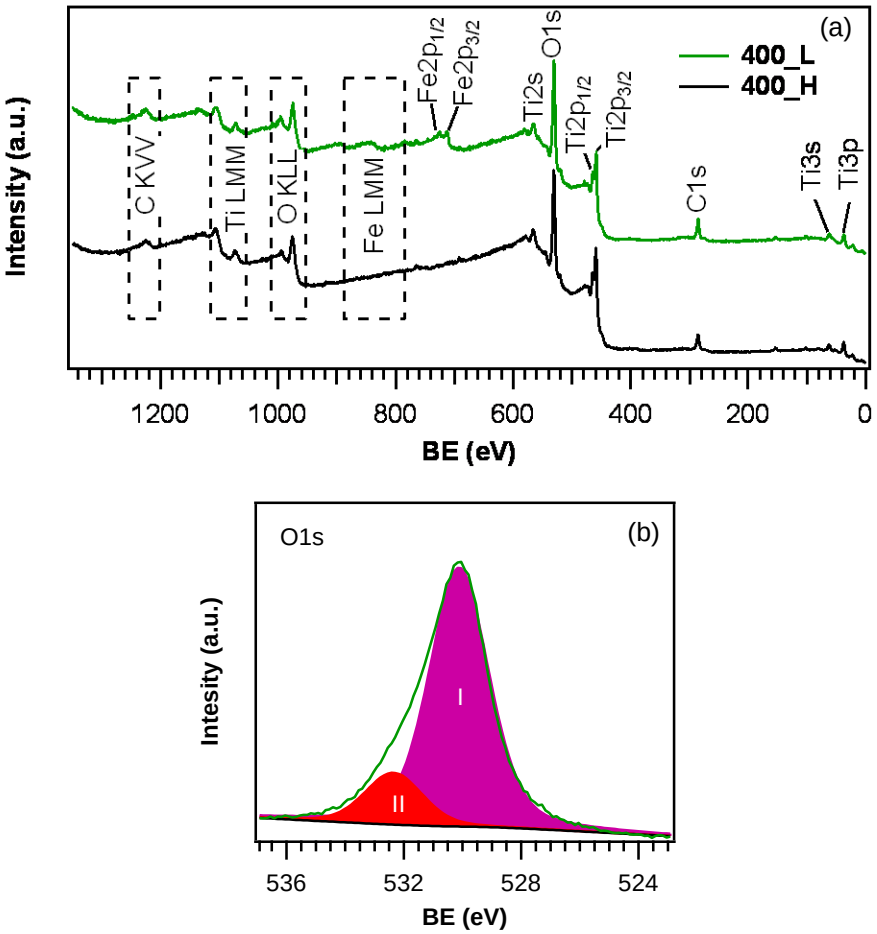

Figure S2. (a) Surface XPS wide-scan spectra for Fe_2O_3-TiO_2 specimens. (b) Surface O1s photoelectron signal for sample **400_L**.

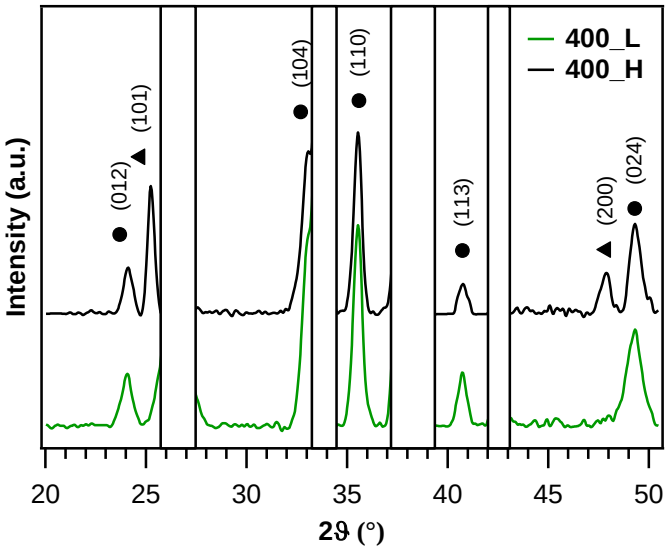

Figure S3. XRD patterns for Fe_2O_3-TiO_2 deposits. The markers indicate α-Fe_2O_3 (*hematite*, ●) and TiO_2 (*anatase*, ◀) reflections, the latter being observed only for specimen **400_H**. For sake of clarity, peaks pertaining to the FTO-coated glass substrate are covered.

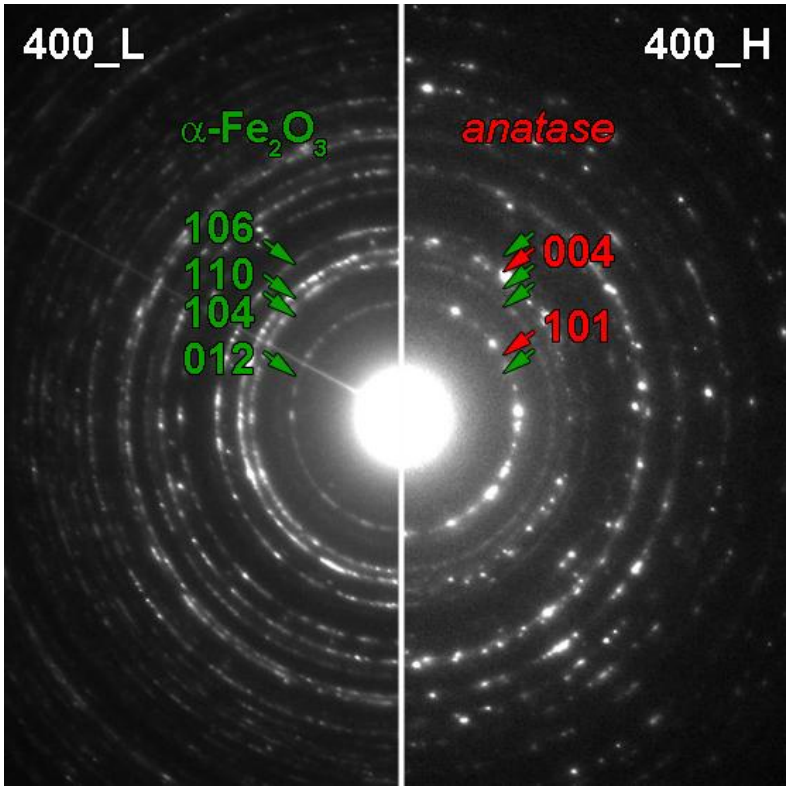

Figure S4. ED ring patterns recorded for samples **400_H** and **400_L** in plane-view orientation. For sample **400_L**, mainly α-Fe_2O_3 reflections are present, together with a few very faint *anatase* reflections. Conversely, in the case of specimen **400_H**, both α-Fe_2O_3 (*hematite*) and TiO_2 (*anatase*) reflections are clearly visible.

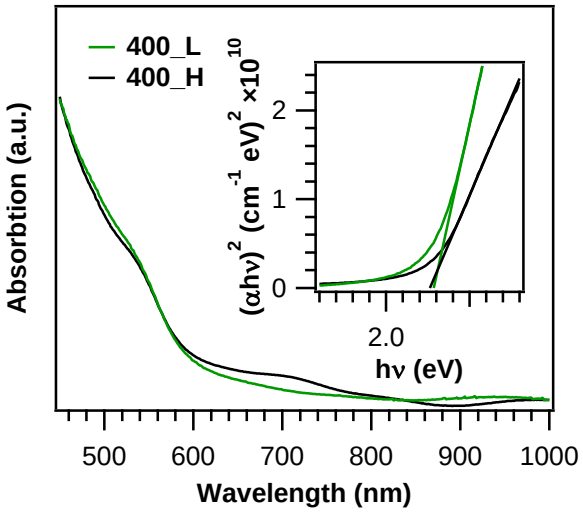

Figure S5. Optical absorption spectra and Tauc plots (inset) for Fe_2O_3-TiO_2 specimens.

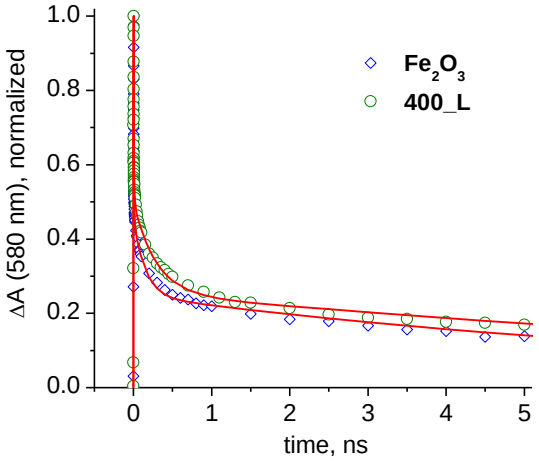

Figure S6. Normalized ns transient absorption decays of Fe_2O_3 and **400_L** Fe_2O_3-TiO_2 specimens probed at λ = 580 nm. The red lines show 4-exponential fits of raw data.

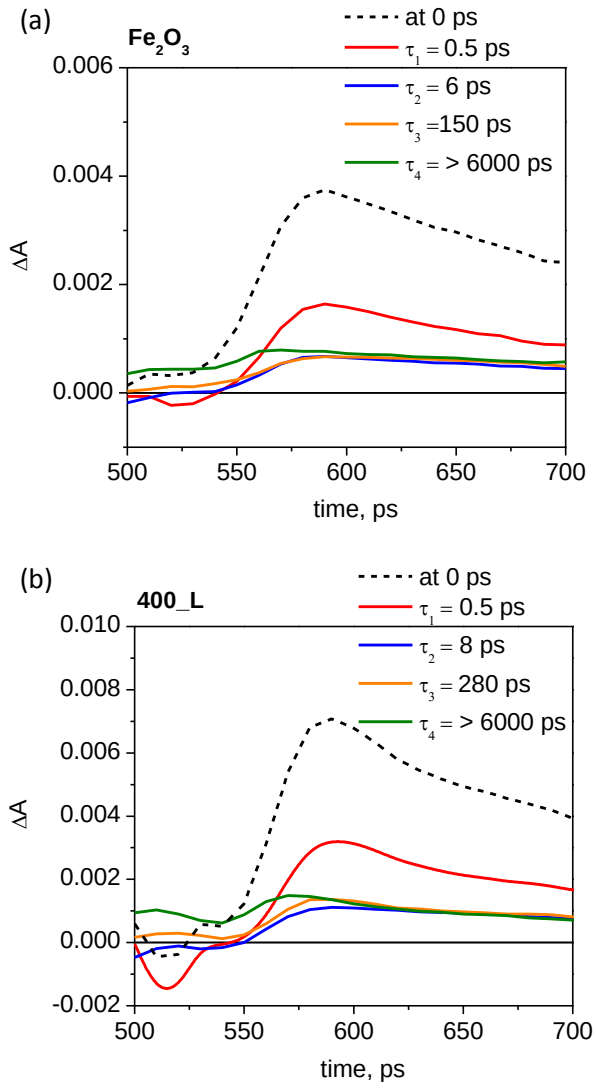

Figure S7. Ultrafast 4-exponential decay component spectra and calculated time-resolved spectrum at 0 ps of: (a) bare Fe_2O_3; (b) **400_L** specimens, at 1.6 V_{RHE}.

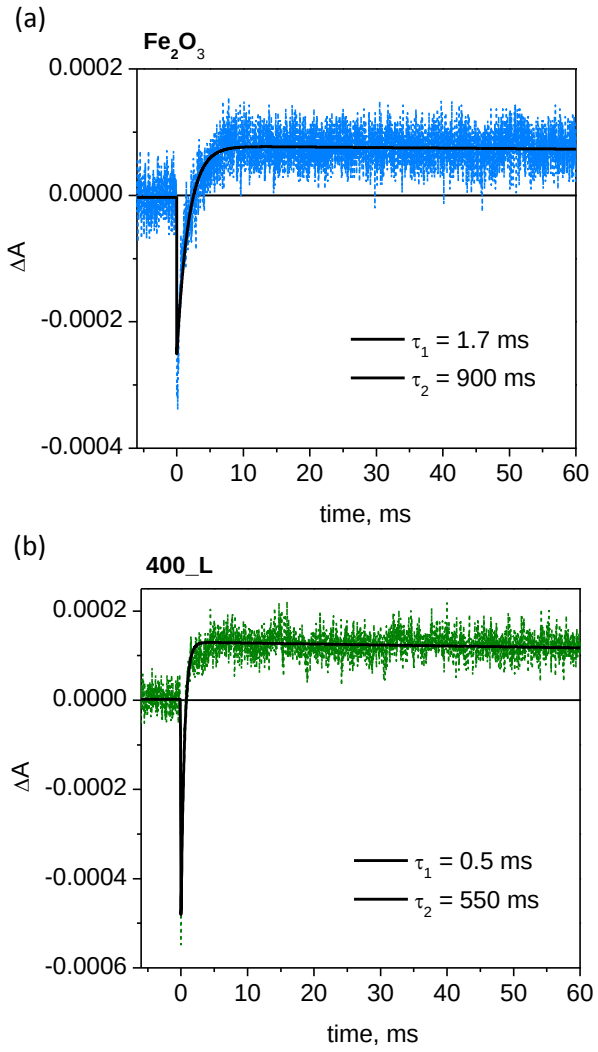

Figure S8. Transient absorption decays of (a) bare Fe_2O_3 and (b) **400_L** specimens, in a microsecond-to-millisecond timescale probed at λ = 580 nm. Black lines correspond to bi-exponential fits of raw data.

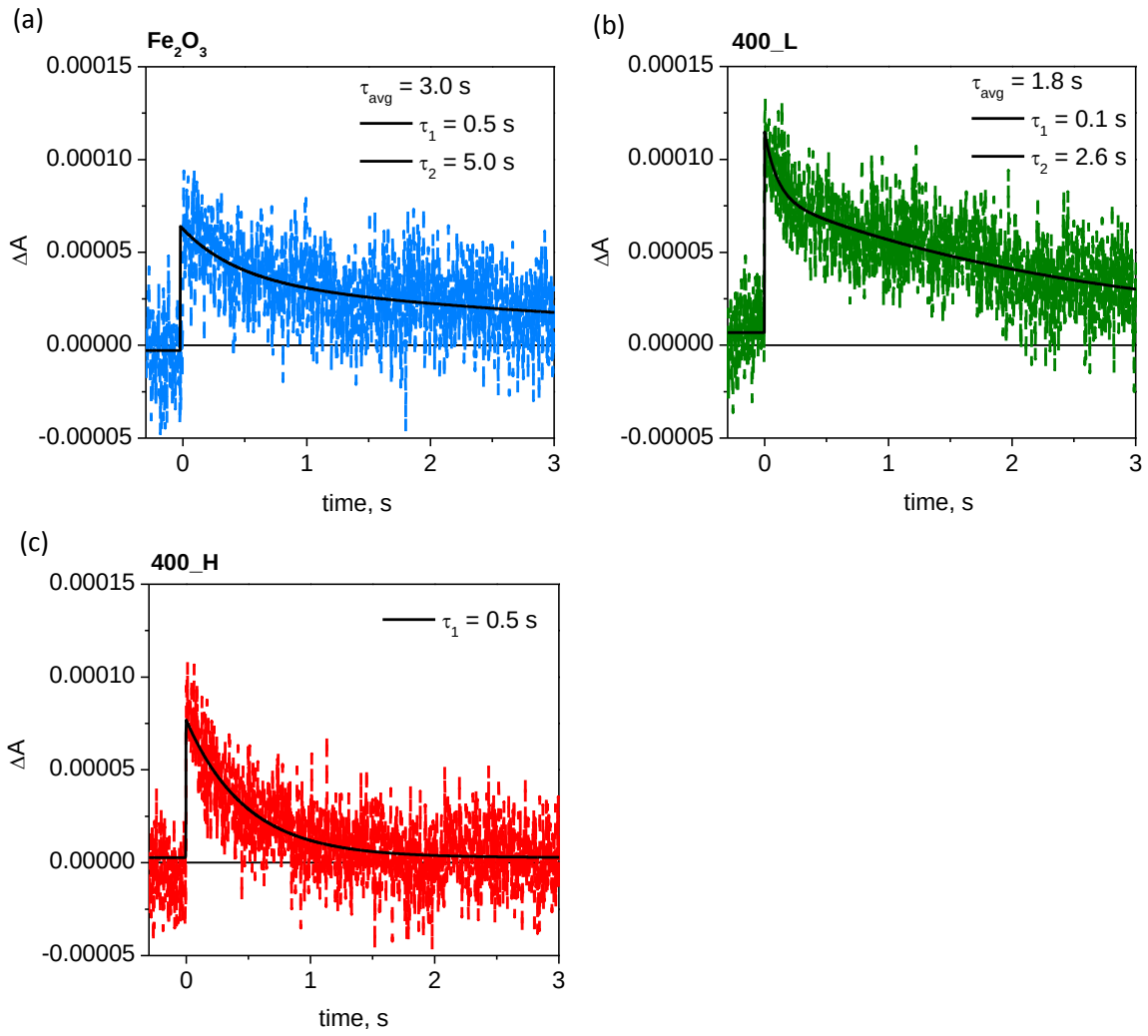

Figure S9. Transient absorption decays of (a) bare Fe_2O_3, (b) **400_L**, and (c) **400_H** specimens in a millisecond-to-second timescale probed at λ = 650 nm. Black curves show exponential fits of raw data (τ_{avg} = weight averaged mean lifetime).